The influence of secondary flows induced by normal stress differences on the shear-induced migration of particles in concentrated suspensions

ARUN RAMACHANDRAN[1] AND DAVID T. LEIGHTON JR[2]

[1]Department of Chemical Engineering, University of California at Santa Barbara, CA 93106, USA

[2]Department of Chemical and Biomolecular Engineering, University of Notre Dame, Notre Dame, IN 46556, USA

It was first demonstrated experimentally by H. Giesekus in 1965 that the second normal stress difference in polymers can induce a secondary flow within the cross-section of a non-axisymmetric conduit. In this paper, we show through simulations that the same may be true for suspensions of rigid non-colloidal particles that are known to exhibit a strong negative second normal stress difference. Typically, the magnitudes of the transverse velocity components are small compared to the average axial velocity of the suspension; but the ratio of this transverse convective velocity to the shear-induced migration velocity is characterized by the shear-induced migration Péclet number χ which scales as B^2/a^2, B being the characteristic length scale of the cross-section and a being the particle radius. Since this Péclet number is kept high in suspension experiments (typically 100 to 2500), the influence of the weak circulation currents on the concentration profile can be very strong, a result that has not been appreciated in previous work. The principal effect of secondary flows on the concentration distribution as determined from simulations using the suspension balance model of Nott & Brady (*J. Fluid Mech.* vol. 275, 1994, p. 157) and the constitutive equations of Zarraga *et al.* (*J. Rheol.* vol. 44, 2000, p. 185) is three-fold. First, the steady-state particle concentration distribution is no longer independent of particle size; rather, it depends on the aspect ratio B/a. Secondly, the direction of the secondary flow is such that particles are swept out of regions of high streamsurface curvature, e.g. particle concentrations in corners reach a minimum rather than the local maximum predicted in the absence of such flows. Finally, the second normal stress differences lead to instabilities even in such simple geometries as plane-Poiseuille flow.

1. Introduction

Over the past three decades, the migration of particles across streamlines in concentrated suspensions has received a great deal of attention. The flow geometries in which particle migration has been studied experimentally are channel flow (Leighton & Acrivos 1987; Schaflinger, Acrivos & Zhang 1990; Koh, Hookham & Leal 1994; Lyon & Leal 1998), Couette flow (Leighton & Acrivos 1987; Tripathi 1998; Shapley, Armstrong & Brown 2002), wide-gap Couette flow (Abbott *et al.* 1991; Tetlow *et al.* 1998), tube flow (Hampton *et al.* 1997), parallel-plate flow (Chapman 1990; Chow *et al.* 1994; Krishnan, Beimfohr & Leighton 1996; Merhi *et al.* 2005; Bricker & Butler 2006), cone and plate flow (Chow *et al.* 1995; Fang *et al.* 2002), eccentric cylinder flow

(Phan-Thien 1995) and resuspension (Leighton & Acrivos 1986; Altobelli, Givler & Fukushima 1991; Chapman & Leighton 1991; Acrivos, Mauri & Fan 1993; Norman, Nayak & Bonnecaze 2005). These studies have shown that particles under shear generally migrate from regions of high concentration to low, from regions of high shear stress to low, and from regions of high streamline curvature to low.

In order to model the migration of particles across streamlines, two major approaches have been employed in the literature: the trajectory model (also known as the diffusive flux model), and the suspension balance model. The trajectory approach is based on a simple view of the kinematics of particle interactions. In this model, when a given test particle in a simple shear flow interacts with another particle approaching from above it, the test particle is displaced downwards. On the other hand, when the second particle approaches the given test particle from below, the test particle is displaced upwards. The microscopic reversibility normally expected for Stokes flow is presumably broken by irreversible non-hydrodynamic interactions via surface roughness (Smart & Leighton 1989; DaCunha & Hinch 1996). If there is a gradient in shear or gradient in concentration of the particles across the streamlines, there is a gradient in the rate of interactions experienced by the particle, which results in migration of the particle across the streamline. In addition, viscosity gradients result in displacement of particles from regions of higher viscosity to regions of lower viscosity. Using these simple intuitive arguments, Leighton & Acrivos (1987) proposed the following particle flux constitutive equation for channel flow

$$N_y = -K_\sigma \frac{\phi^2}{\tau} \frac{\partial \tau}{\partial y} \dot\gamma a^2 - K_\parallel \frac{\phi^2}{\mu} \frac{\partial \mu}{\partial \phi} \frac{\partial \phi}{\partial y} \dot\gamma a^2. \tag{1.1}$$

The shear-induced gradient diffusion coefficient thus scales as $\dot\gamma a^2$, where $\dot\gamma$ is the local shear rate, a is the particle radius, τ is the magnitude of the local shear stress and μ is the viscosity of the suspension as a function of the volume fraction ϕ. The parameters K_σ and $K_\parallel$ were experimentally estimated to be 0.6 and 0.7, respectively, at 45 % volume fraction. This model was extended to more general two-dimensional shear flows by Phillips *et al.* (1992).

$$N = -K_c a^2 \left[\phi^2 \nabla \dot\gamma + \dot\gamma \phi \nabla \phi \right] - K_\eta \frac{\phi^2}{\mu} \frac{\partial \mu}{\partial \phi} \dot\gamma a^2 \nabla \phi. \tag{1.2}$$

The constants K_c and K_η were empirically determined to be 0.43 and 0.65, respectively. The model was further modified by Tetlow *et al.* (1998) by determining K_c and K_η as linear functions of ϕ, but retained its essential form. Since the model devised by Leighton & Acrivos was applicable only to simple planar unidirectional flows, the extension by Phillips *et al.* to more complicated flows implicitly assumes that particle migration is isotropic. Since this model always predicts migration down a shear gradient, it is unable to explain the apparent lack of migration in parallel-plate flow (Chapman 1990; Merhi *et al.* 2005; Bricker & Butler 2006) in which the shear rate increases radially outwards, and the outward migration of particles in cone and plate flow (Chow *et al.* 1995; Fang *et al.* 2002), in which the stress is constant. To account for the effects of streamline curvature, Krishnan *et al.* (1996) proposed an additional particle flux term in the diffusive flux model which causes particle migration owing to gradients in streamline curvature. Their modified constitutive equation for the radial flux balance in the parallel-plate geometry is

$$N_r = K_{r\perp} \frac{\phi^2}{r} \dot\gamma a^2 - K_{\sigma\perp} \phi^2 a^2 \frac{\partial \dot\gamma}{\partial r} - K_\perp \frac{\phi^2}{\mu} \frac{\partial \mu}{\partial \phi} \frac{\partial \phi}{\partial r} \dot\gamma a^2. \tag{1.3}$$

The symbol $\perp$ denotes migration perpendicular to the plane of shear. The constant $K_{r\perp}$ was taken to be 0.7, thus balancing the shear rate gradient term exactly. Merhi *et al.* (2005) suggested a slightly greater value for $K_{r\perp}$, leading to a small outward radial migration. A similar curvature term can be added to the radial flux balance in the case of wide-gap Couette flow. However, in this case, the migration is *in* the plane of shear from streamlines of higher curvature to streamlines of lower curvature, and therefore should be characterized by a different coefficient which also may be a function of concentration. Thus, it can be seen that although the diffusive flux model is simple and intuitive, it requires numerous coefficients which must be determined empirically.

The suspension balance model, on the other hand, provides a more unified approach for describing particle migration (e.g. Nott & Brady 1994; Morris & Boulay 1999; Fang *et al.* 2002). In this model, particle migration is ascribed to gradients in the particle stress tensor Σ_{ij}^{p}. As described in §2, with the inclusion of the anisotropic terms in the particle stress tensor, the suspension balance model successfully explains the migration behaviours in all perturbations of simple shear flows, including the curvature-induced migration in the parallel-plate and cone and plate geometries. What has not been previously appreciated is the direct effect of the non-Newtonian particle stress on the convection within the cross-section of a conduit.

Consider the simple example of unidirectional flow of a suspension through a conduit of arbitrary cross-section. The total stress Σ_{ij} in a suspension is the sum of the stress contributions from the suspending liquid and the particles. At high concentrations, the particle stress and consequently the total stress is anisotropic in nature, rendering concentrated suspensions non-Newtonian. If the particle stress tensor is taken to be isotropic (thus assuming that the suspension is Newtonian), it can be shown that the cross-sectional components of velocity are identically zero under fully developed flow conditions. However, if the anisotropy of the particle stress tensor is factored in, then this trivial solution no longer satisfies the flow equations, the components of the velocity vector in the plane of the cross-section of the conduit are necessarily non-zero, and a helicoidal flow of the suspension results at steady state.

The existence of such flows is already well established in polymer literature. Green & Rivlin (1956) were the first to conclude that it is, in general, not possible to have steady and rectilinear flow of a viscoelastic polymer through a channel whose cross-section is not circular. They used a fourth-order fluid model to show that the second normal stress differences could produce a secondary flow in the steady flow of the fluid in a non-circular conduit. This was first verified experimentally by Giesekus (1965). He injected a stream of dyed polymer into a 5 % solution of polyacrylamide flowing in an elliptical channel and observed that the dye exhibited a swirling motion as the polymer flowed through the channel at a Reynolds number of order 10^{-4}. Secondary currents in polymer flows were also studied experimentally by Semjonow (1967) and Dodson, Townsend & Walters (1974) by similar visual techniques. Dooley and colleagues have demonstrated the strong impact of secondary flows in the coextrusion process by studying the deformation of the interface between two contrastingly pigmented layers of low-density polyethylene during flow through a square channel (Debbaut *et al.* 1997; Debbaut & Dooley 1999). Brady & Carpen (2002) also showed that in two-layer Couette flow and the falling film geometry, the flow field for a suspension of non-colloidal particles (modelled with constant concentration) was unstable to spanwise perturbations, the instability being driven by a second normal stress difference jump between the suspension and Newtonian phases. The secondary

currents in Brady & Carpen appear as a perturbation from an unstable steady state that does not have any circulation. However, in this paper, we demonstrate that the steady-state distribution itself is accompanied by secondary currents for suspension flow through conduits. The similarity between the secondary motions induced in viscoelastic polymer flow and suspension flow in channels is that their magnitudes are inherently weak, typically two to three orders of magnitude lower than the axial velocity. The subtle difference, however, is that in suspension flow, these weak secondary flows are linked to the concentration distribution equation by a convective term that scales as the shear-induced migration Péclet number $\chi = B^2/a^2$ which, for typical experimental conditions, is of order 10^2 or higher, B being a characteristic dimension of the cross-section. In this paper, we demonstrate the effects that these circulation velocities may have on the steady-state particle distribution. Note that the Péclet number we refer to in this paper is not the ratio $\dot{\gamma}a^2/(kT/6\pi\mu a)$ of hydrodynamic to Brownian diffusivity, but rather the ratio of the convective velocity scaling to the shear-induced diffusive velocity as defined in (4.5).

This paper is arranged as follows. In §2, the suspension balance model is formulated using the constitutive equations of Zarraga, Hill & Leighton (2000), and the capability of this anisotropic model for describing particle migration behaviours in curvilinear flows is described. In §3, the effect of the geometry of the conduit cross-section on the velocity distribution is analysed assuming a constant concentration throughout the cross-section of the conduit. This would be the velocity distribution expected in the case of a homogeneous suspension of very small particles for which the long time required to approach the non-uniform steady concentration distribution has not yet elapsed. In §4, the effects of particle stress anisotropy on the concentration and velocity distributions, respectively, are integrated; that is, the full solutions of the governing equations for fully developed flow in elliptical, rectangular (with and without sidewalls) and wedge-shaped cross-sections are analysed. We conclude by summarizing our results.

2. Concentration profiles in the absence of secondary flows

The suspension balance approach for modelling the particle and velocity distributions in concentrated suspension flows (Jenkins & McTigue 1990; Nott & Brady 1994; Morris & Boulay 1999; Fang *et al.* 2002) performs mass and momentum balances on both particulate and suspension phases. The coupling between the two momentum balances is achieved via the particle stress tensor Σ_{ij}^p, and any non-zero gradients of the particle stress tensor result in particle migration and in a net normal stress being exerted on the fluid phase.

In a suspension, as shown by Nott & Brady (1994), the flux of particles is given by the average motion of all the particles

$$N_i = u_i\phi + \langle M_{ij}F_j\rangle\phi, \tag{2.1}$$

where $\langle\cdot\rangle$ denotes an ensemble average over all the particles contained in a volume V, u_i is the volume averaged suspension velocity and M_{ij} is the mobility function that determines the velocity of the particles in response to a force F_i. Invoking the approximation that the ensemble average of the mobility multiplied by the force on the particles is equal to the product of the separate ensemble averages of the mobility and the force (Nott & Brady 1994), i.e.

$$\langle M_{ij}F_j\rangle \approx \langle M_{ij}\rangle\langle F_j\rangle, \tag{2.2}$$

and approximating the mobility $\langle M_{ij} \rangle$ by an isotropic function that describes the hindered motion of a particle surrounded by other particles (namely the hindered Stokes sedimentation velocity),

$$\langle M_{ij} \rangle \approx \frac{1}{6\pi\mu_0 a} f \delta_{ij}, \tag{2.3}$$

the particle flux is obtained as

$$N_i = u_i\phi + \frac{1}{6\pi\mu_0 a} f \langle F_i \rangle \phi. \tag{2.4}$$

Note that the approximations in (2.2) and (2.3) are rigorously valid for a dilute suspension of particles which interact solely through a long-range repulsive hard-sphere potential. They also appear, however, to be remarkably robust even for highly concentrated anisotropic suspensions (Zarraga & Leighton 2001). Applying a momentum balance over the particulate phase at steady state under creeping flow conditions, we obtain

$$\frac{\partial \Sigma_{ij}^p}{\partial x_j} = \langle F_i \rangle \frac{\phi}{\frac{4}{3}\pi a^3}, \tag{2.5}$$

where $\phi/(4/3)\pi a^3$ is the number of particles per unit volume. In this paper, we assume that the particles are neutrally buoyant so that there are no body forces applied on the particulate phase. Combining (2.4) and (2.5), the particulate flux is given by

$$N_i = \underbrace{u_i\phi}_{\text{Convective flux } N_{C_i}} + \underbrace{\frac{2}{9}\frac{a^2}{\mu_0} f \frac{\partial \Sigma_{ij}^p}{\partial x_j}}_{\text{Shear-induced diffusive flux } N_{D_i}}. \tag{2.6}$$

Thus, as was shown by Nott & Brady (1994), the shear-induced diffusive particle flux is directly proportional to the gradients in the particle stress tensor Σ_{ij}^p.

The model is completed by assuming an appropriate constitutive equation for the particle stress. Several constitutive equations have been developed to describe the particle stress in terms of particle concentration and the shear geometry. Nott & Brady developed a constitutive model in which they defined a suspension temperature and pressure in terms of velocity fluctuations akin to granular flow, but they assumed the suspension temperature and pressure to be isotropic. Mills & Snabre (1995) derived an isotropic model relating the particle stress to the mean stress in the suspension by considering the lubrication interaction between colliding spheres. Unfortunately, these constitutive equations have the same deficiency as any isotropic model: failure to explain the observed particle migration behaviours in geometries with curvature (e.g. parallel-plate and cone and plate flow).

Rather than using the temperature formulation of the suspension balance model (Nott & Brady 1994) where the particle pressure is related to local velocity fluctuations, we find it convenient in this paper to use the measurements of Zarraga *et al.* (2000) directly for describing the particle stresses, yielding a model with zero adjustable parameters much like the approach of Morris & Boulay (1999). Zarraga *et al.* (2000) characterized the dimensionless normal stresses $(N_1 - N_2)/\tau$, N_1/τ and $(N_2 + 1/2N_1)/\tau$ in the parallel-plate, cone and plate and rotating rod geometries-respectively. These normal stress difference results were connected with the particle stress $-\Sigma_{pp}^p/\tau$ extracted from the data collected by Acrivos *et al.* (1993) for resuspension in a Couette device. Their results for the particle stress in the flow direction $\boldsymbol{m}$, velocity gradient

direction n and vorticity direction p are as follows

$$\left.\begin{array}{l} \Sigma^P_{mm} = -1.15\alpha\tau = -(1-b)\alpha\tau, \\ \Sigma^P_{nn} = -\alpha\tau, \\ \Sigma^P_{pp} = -0.46\alpha\tau = -(1+d)\alpha\tau. \end{array}\right\} \tag{2.7}$$

In this model, α is the reduced second normal stress given by

$$\alpha = 2.17\phi^3 \exp(2.34\phi) \tag{2.8}$$

with $b = -0.15$ and $d = -0.54$ being the first and second normal stress difference coefficients normalized by the total particle stress in the gradient direction, i.e. $b = N_1/\alpha\tau$ and $d = N_2/\alpha\tau$. In practice, of course, the structure (and hence anisotropy) of a suspension depends on the concentration ϕ. Zarraga *et al.*, however, found their data to be reasonably described by taking b and d to be constant. Also, the second normal-stress-difference coefficient was observed to be larger than the first. The local shear stress τ is defined as

$$\tau = \mu_0\mu_r\dot{\gamma}, \tag{2.9}$$

where μ_0 is the viscosity of the suspending fluid and $\dot{\gamma}$ is the local shear rate. For a general shear flow, $\dot{\gamma}$ is given by

$$\dot{\gamma} = \sqrt{2e_{ij}e_{ji}}, \tag{2.10}$$

e_{ij} being the rate of strain tensor defined as

$$e_{ij} = \frac{1}{2}\left(\frac{\partial u_i}{\partial x_j} + \frac{\partial u_j}{\partial x_i}\right), \tag{2.11}$$

μ_r is the suspension relative viscosity given by the correlation (Zarraga *et al.* 2000)

$$\mu_r = \frac{\exp(-2.34\phi)}{(1-\phi/\phi_m)^3}, \tag{2.12}$$

where $\phi_m = 0.62$ is the maximum packing fraction. The approach of Morris & Boulay (1999) is equivalent to that determined from rheological measurements described here except for a different constitutive relationship for α and where $b = -0.25$ and $d = -0.375$. The particle stress tensor is thus written as

$$\begin{aligned} \Sigma^P_{ij} &= \Sigma^P_{mm}m_im_j + \Sigma^P_{nn}n_in_j + \Sigma^P_{pp}p_ip_j + 2\mu_0(\mu_r - 1)e_{ij} \\ &= -\alpha\tau[(1-b)m_im_j + n_in_j + (1+d)p_ip_j] + 2\mu_0(\mu_r - 1)e_{ij} \\ &= -\alpha\tau H_{ij} + 2\mu_0(\mu_r - 1)e_{ij}. \end{aligned} \tag{2.13}$$

H_{ij} is a symmetric tensor that represents the flow geometry weighted with the normal stress difference coefficients.

$$H_{ij} = (1-b)m_im_j + n_in_j + (1+d)p_ip_j. \tag{2.14}$$

Now let us consider steady-state concentration distributions in viscometric geometries. At steady state, it is common to assume that both convective and diffusive particle fluxes are identically zero. Under these conditions, the steady-state concentration profile can be obtained from the simple equation

$$\frac{\partial \Sigma^P_{ij}}{\partial x_j} = 0. \tag{2.15}$$

As we shall see in §§ 3 and 4, this assumption is true for isotropic suspension models and for anisotropic suspensions only for the commonly used viscometric geometries (parallel-plate flow, Couette flow, cone and plate flow, etc.) that are discussed in this section. This assumption will be shown in §4 to break down for more complicated geometries. First, let us examine migration in viscometric flows under the assumption that the particle stress tensor is isotropic. In this case, the geometry tensor H_{ij} reduces to

$$H_{ij}^{(I)} = \tfrac{1}{3} \left[(1-b) + 1 + (1+d) \right] \delta_{ij} = 0.87 \delta_{ij}. \tag{2.16}$$

The steady-state solution to the particle flux balance equations for fully developed unidirectional flow through any geometry with arbitrary (but uniform) cross-section is very simple with this isotropic approximation:

$$\alpha \tau = \text{constant}, \tag{2.17}$$

i.e. the particle stress is predicted to be identical at all points in the cross-section. Since α is a monotonically increasing function of ϕ, the concentration in any region in the conduit is inversely related to the shear stress in that region.

The simple approach described above is strictly a result of ignoring the anisotropy of the particle stress tensor. Unfortunately, this solution holds true only for the case of plane Poiseuille flow in a channel without sidewalls where the streamlines are not curved. The outward migration of particles observed in the cone and plate and parallel-plate geometries cannot be explained by the above solution. Even for circular tubes, the particle migration towards the centre of the tube is stronger than that calculated from the isotropic model. To see how anisotropy influences migration, consider the case of migration in a circular tube (e.g. Fang *et al.* 2002).

$$N_r = \frac{2}{9} \frac{a^2}{\mu_0} f \left[\frac{1}{r} \frac{\partial}{\partial r} \left(r \Sigma_{rr}^p \right) - \frac{\Sigma_{\theta\theta}^p}{r} \right] = 0. \tag{2.18}$$

For this geometry, the r-direction represents the velocity gradient direction and the θ direction represents the vorticity direction. Therefore, from (2.7), we have

$$\Sigma_{rr}^p = -\alpha\tau, \quad \Sigma_{\theta\theta}^p = -(1+d)\alpha\tau. \tag{2.19}$$

Substitution of these particle stress components into (2.18) yields

$$\frac{1}{r} \frac{\partial}{\partial r} (r\alpha\tau) - (1+d)\frac{\alpha\tau}{r} = 0 \tag{2.20}$$

which can be simplified to

$$\underbrace{\frac{\partial \alpha\tau}{\partial r}}_{\text{Stress gradient term}} - \underbrace{d \frac{\alpha\tau}{r}}_{\text{Curvature term}} = 0. \tag{2.21}$$

Equation (2.21) can be solved to yield

$$\alpha\tau = \text{constant} \times r^d. \tag{2.22}$$

Since d is negative, this results in stronger radial concentration gradients than for the isotropic model (which predicts a constant particle pressure).

As shown by Morris & Boulay (1999) and Fang *et al.* (2002), the inclusion of the particle stress anisotropy into the constitutive equation also enables the model to explain the observed concentration distributions in the torsional parallel-plate and

cone and plate geometries. For example, in the parallel-plate geometry, a flux balance in the r-direction at steady state gives

$$N_r = \frac{2}{9}\frac{a^2}{\mu_0} f \left[\frac{1}{r}\frac{\partial}{\partial r}\left(r \Sigma_{rr}^p \right) - \frac{\Sigma_{\theta\theta}^p}{r} \right] = 0. \tag{2.23}$$

In this geometry, the θ-direction represents the flow direction, the z-direction is the velocity gradient direction, while the r-direction is the vorticity direction. Using the constitutive equations of Zarraga *et al.* (2000), we have from (2.7) and (2.13) that

$$\Sigma_{rr}^p = -(1+d)\alpha\tau, \qquad \Sigma_{\theta\theta}^p = -(1-b)\alpha\tau. \tag{2.24}$$

Also, the shear rate increases linearly with the radial position r. This yields the radial concentration gradient as

$$\frac{\partial\phi}{\partial r} = -\frac{1+b+2d}{1+d}\frac{\alpha\mu_r}{(\alpha\mu_r)'}\frac{1}{r}, \tag{2.25}$$

where the prime denotes the derivative with respect to concentration. Integrating (2.25) with r and using the measured dependences of α and μ_r yields the concentration distribution up to an arbitrary constant.

$$\phi = \frac{c\phi_m r^{-(1+b+2d)/3(1+d)}}{\phi_m + c r^{-(1+b+2d)/3(1+d)}}. \tag{2.26}$$

This constant c is set by choosing the average concentration in the device. The exponent $-(1+b+2d)/3(1+d)$ is equal to 0.17 using the values for the normal stress difference coefficients from (2.7). We can see that the model predicts a very weak outward migration of particles, which is consistent with the apparent lack of migration observed in parallel-plate experiments (e.g. Chapman 1990). It is still not clear whether migration actually occurs in the parallel-plate geometry. Merhi *et al.* (2005) reported the experimental measurement of an outward migration of particles in their parallel-plate experiments. This could not be confirmed by Bricker & Butler (2006), who did not observe any change in the apparent viscosity of the suspension during their parallel-plate measurements. The model does, however, correctly predict the outward migration of particles in the cone and plate geometry reported by Chow *et al.* (1995) and Fang *et al.* (2002).

A compact and sensitive way of summarizing the steady-state concentration distributions in viscometric flows is to determine the dimensionless concentration gradient $r\partial\phi/\partial r$ described in table 1 using the constitutive equations of Zarraga *et al.* (2000) for these geometries. Note that the dimensionless concentration gradient can be predicted with no adjustable parameters using the suspension balance formulation discussed above. The results from various experimental studies in different geometries are presented in figure 1. We see that the agreement is excellent within the experimental scatter of these studies.

In the viscometric geometries considered above, both components of the particle flux vector were zero at steady state, leading to a simple prediction for the steady concentration distribution even including the effects of anisotropy. We now consider the more complex situation of unidirectional flow through a conduit of arbitrary cross-section where this is no longer the case.

Geometry	Dimensionless concentration gradient
Channel flow	$y\dfrac{\partial\phi}{\partial y} = -\dfrac{\alpha}{\alpha'}$
Tube Poiseuille flow	$r\dfrac{\partial\phi}{\partial r} = -(1-d)\dfrac{\alpha}{\alpha'}$
Wide gap Couette flow	$r\dfrac{\partial\phi}{\partial r} = (2-b)\dfrac{\alpha}{\alpha'}$
Cone and plate flow	$r\dfrac{\partial\phi}{\partial r} = -\dfrac{b+2d}{1+d}\dfrac{\alpha\mu_r}{(\alpha\mu_r)'}$
Parallel plate geometry	$r\dfrac{\partial\phi}{\partial r} = -\dfrac{1+b+2d}{1+d}\dfrac{\alpha\mu_r}{(\alpha\mu_r)'}$

TABLE 1. The dimensionless concentration gradients from the suspension balance model of Nott & Brady (1994) with the consitutive equations of Zarraga *et al.* (2000) in different viscometric geometries.
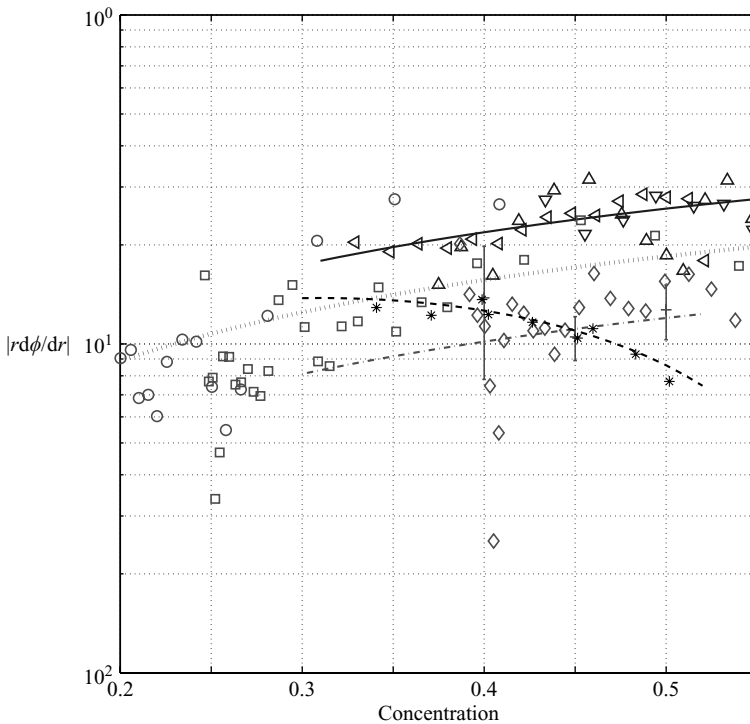
FIGURE 1. A comparison between the experimental data and theoretical prediction of the dimensionless concentration gradient in various geometries. Wide gap Couette data of Phillips *et al.* (1992): ◁, 45 %; △, 50 %; ▽, 55 %; — theory. Tube data obtained by Hampton *et al.* (1997): ○, 20 %; □, 30 %; ◇, 45 %; ...., theory. Plane Poiseuille flow of Leighton & Acrivos (1987): +, 45 %, − · −, theoretical result. Truncated cone and plate data of Chow *et al.* (1995): ∗, 50 %; − − −, theory.

3. The origin of secondary flows in particulate suspensions

Consider the flow of a suspension of rigid non-colloidal particles through a conduit of arbitrary cross-section. Let the z-axis represent the axial direction and x and y

represent the cross-sectional coordinates. Since our focus in this work is on the fully developed distributions of particle concentration ϕ and velocities $[u, v, w]$ within the cross-section (x, y-plane), we invoke the quasi-steady-state approximation, i.e. all variations in the axial direction are ignored.

The variables in this problem are rendered dimensionless as follows:

$$[x, y, z] = [x^*, y^*, z^*)B, \quad [u, v, w] = [u^*, v^*, w^*)GB^2/\mu_0, \quad P = P^*GB. \quad (3.1)$$

Here, the pressure P in the conduit is rendered dimensionless by the scaling GB, G being the pressure gradient applied in the flow direction. The velocity components u, v and w are non-dimensionalized by the scaling $U_c = GB^2/\mu_0$, where B is the characteristic length scale in the cross-section and μ_0 is the viscosity of the suspending fluid. For convenience, the asterisks accompanying the non-dimensionalized variables will be dropped hereinafter. Also, in all subsequent equations, $[x_1, x_2, x_3] \equiv [x, y, z]$ and $[u_1, u_2, u_3] \equiv [u, v, w]$.

The continuity equation is

$$\frac{\partial u}{\partial x} + \frac{\partial v}{\partial y} = 0. \quad (3.2)$$

A momentum balance over the suspension yields

$$\frac{\partial \Sigma_{ij}}{\partial x_j} = 0. \quad (3.3)$$

Here, the total suspension stress Σ_{ij} is given by

$$\Sigma_{ij} = -P\delta_{ij} + 2e_{ij} + \Sigma_{ij}^p. \quad (3.4)$$

The particle stress tensor Σ_{ij}^p is defined using (2.13) as

$$\Sigma_{ij}^p = -\alpha\tau H_{ij} + 2(\mu_r - 1)e_{ij}. \quad (3.5)$$

Combining (3.3)–(3.5), we obtain

$$\frac{\partial}{\partial x_j}(2\mu_r e_{ij}) = \frac{\partial P}{\partial x_i} + \frac{\partial}{\partial x_j}(\alpha\tau H_{ij}). \quad (3.6)$$

The tensor H_{ij} as defined in (2.14) represents the geometry of the flow field. If the flow were purely unidirectional, the flow m_i, velocity gradient n_i and the vorticity p_i directions would be given by

$$\left.\begin{array}{l} m_i = \delta_{i3}, \\ n_i = \dfrac{\partial w/\partial x_i}{\sqrt{\partial w/\partial x_k\,\partial w/\partial x_k}}, \\ p_i = \dfrac{\Omega_i}{\sqrt{\Omega_k\Omega_k}}, \end{array}\right\} \quad (3.7)$$

where Ω_i is the vorticity vector given by

$$\Omega_i = \epsilon_{ij3}\frac{\partial w}{\partial x_j}. \quad (3.8)$$

Using (2.14), the geometry tensor can be written for purely unidirectional flows as

$$H_{ij} = (1 - b)\delta_{i3}\delta_{j3} + n_i n_j + (1 + d)p_i p_j. \quad (3.9)$$

The secondary currents induced by the non-Newtonian rheology are very small in magnitude compared to the axial velocity, and thus we may ignore their effect on the

flow geometry tensor to leading order. Therefore, the expression for H_{ij} in (3.9) may also be used for the quasi-unidirectional flows expected here.

Since the velocity gradient and vorticity vectors defined above are always orthogonal, we can write

$$\delta_{i3}\delta_{j3} + n_i n_j + p_i p_j = \delta_{ij}. \tag{3.10}$$

The geometry tensor thus reduces to

$$H_{ij} = \delta_{ij} - b\delta_{i3}\delta_{j3} + d\frac{\Omega_i \Omega_j}{\Omega_k \Omega_k}. \tag{3.11}$$

The stress τ is defined as

$$\tau = \mu_r \dot{\gamma}, \tag{3.12}$$

while $\dot{\gamma}$ is defined to leading order as

$$\dot{\gamma} = \sqrt{\left(\frac{\partial w}{\partial x}\right)^2 + \left(\frac{\partial w}{\partial y}\right)^2}. \tag{3.13}$$

Because of the assumption of quasi-unidirectional flow, the total pressure P in the system can be decomposed into an axial component $\overline{P}$ that varies linearly in axial position (constant axial pressure gradient) and a cross-sectional component $\hat{P}$.

$$P(x, y, z) = \overline{P}(z) + \hat{P}(x, y) = -z + \hat{P}(x, y). \tag{3.14}$$

With this simplification, the momentum equations in the x-, y- and z-directions can be written separately as

$$\frac{\partial}{\partial x}\left[2\mu_r \frac{\partial u}{\partial x}\right] + \frac{\partial}{\partial y}\left[\mu_r\left(\frac{\partial u}{\partial y} + \frac{\partial v}{\partial x}\right)\right]$$
$$= \frac{\partial \hat{P}}{\partial x} + \frac{\partial}{\partial x}(\alpha\tau H_{11}) + \frac{\partial}{\partial y}(\alpha\tau H_{12}), \tag{3.15a}$$

$$\frac{\partial}{\partial x}\left[\mu_r\left(\frac{\partial u}{\partial y} + \frac{\partial v}{\partial x}\right)\right] + \frac{\partial}{\partial y}\left[2\mu_r \frac{\partial v}{\partial y}\right]$$
$$= \frac{\partial \hat{P}}{\partial y} + \frac{\partial}{\partial x}(\alpha\tau H_{21}) + \frac{\partial}{\partial y}(\alpha\tau H_{22}), \tag{3.15b}$$

$$\frac{\partial}{\partial x}\left(\mu_r \frac{\partial w}{\partial x}\right) + \frac{\partial}{\partial y}\left(\mu_r \frac{\partial w}{\partial y}\right) = -1. \tag{3.15c}$$

Consider the case where the concentration distribution in the cross-section of the conduit is uniform. This situation is physically realizable in the limit of very large conduit to particle size ratios, i.e. $B/a \gg 1$. In this limit, the characteristic shear-induced migration velocity of the particle is very small, and it takes extremely long channels for the concentration distribution to evolve from the uniform distribution at the inlet to the non-uniform fully developed concentration distribution. Therefore, the concentration profile can be assumed to be constant at the inlet concentration ϕ_f and axially invariant in this asymptotic limit. With this assumption, the momentum equations are simplified considerably.

$$\nabla^2 u = \frac{1}{\mu_r}\frac{\partial \hat{P}}{\partial x} + \alpha\left[\frac{\partial(\dot{\gamma}H_{11})}{\partial x} + \frac{\partial(\dot{\gamma}H_{12})}{\partial y}\right], \tag{3.16a}$$

$$\nabla^2 v = \frac{1}{\mu_r} \frac{\partial \hat{P}}{\partial y} + \alpha \left[\frac{\partial (\dot{\gamma} H_{21})}{\partial x} + \frac{\partial (\dot{\gamma} H_{22})}{\partial y} \right], \tag{3.16b}$$

$$\nabla^2 w = -\frac{1}{\mu_r}. \tag{3.16c}$$

Consider the governing equations for u and v in (3.16a) and (3.16b), respectively. The driving terms for these velocity components in the conduit are gradients in the particle stress. Note that the isotropic part of the particle stress tensor can always be balanced by an appropriate pressure gradient by defining an augmented pressure $\tilde{P}$.

$$\tilde{P} = \hat{P} + \alpha \tau. \tag{3.17}$$

The momentum equations in the x- and y-directions can be recast in terms of the augmented pressure $\tilde{P}$.

$$\nabla^2 u - \frac{1}{\mu_r} \frac{\partial \tilde{P}}{\partial x} = \alpha d \left[\frac{\partial}{\partial x} \left(\dot{\gamma} \frac{\Omega_1^2}{|\boldsymbol{\Omega}|^2} \right) + \frac{\partial}{\partial y} \left(\dot{\gamma} \frac{\Omega_1 \Omega_2}{|\boldsymbol{\Omega}|^2} \right) \right], \tag{3.18a}$$

$$\nabla^2 v - \frac{1}{\mu_r} \frac{\partial \tilde{P}}{\partial y} = \alpha d \left[\frac{\partial}{\partial x} \left(\dot{\gamma} \frac{\Omega_2 \Omega_1}{|\boldsymbol{\Omega}|^2} \right) + \frac{\partial}{\partial y} \left(\dot{\gamma} \frac{\Omega_2^2}{|\boldsymbol{\Omega}|^2} \right) \right]. \tag{3.18b}$$

The definition of H_{ij} in (3.11) has been applied in the above equations. If we differentiate (3.18a) with respect to y, (3.18b) with respect to x and subtract the two, we obtain

$$\begin{aligned}
\nabla^2 \left(\frac{\partial u}{\partial y} - \frac{\partial v}{\partial x} \right) = -\nabla^2 \omega &= \alpha d \frac{\partial}{\partial y} \left[\frac{\partial}{\partial x} \left(\dot{\gamma} \frac{\Omega_1^2}{|\boldsymbol{\Omega}|^2} \right) + \frac{\partial}{\partial y} \left(\dot{\gamma} \frac{\Omega_1 \Omega_2}{|\boldsymbol{\Omega}|^2} \right) \right] \\
&\quad - \alpha d \frac{\partial}{\partial x} \left[\frac{\partial}{\partial x} \left(\dot{\gamma} \frac{\Omega_2 \Omega_1}{|\boldsymbol{\Omega}|^2} \right) + \frac{\partial}{\partial y} \left(\dot{\gamma} \frac{\Omega_2^2}{|\boldsymbol{\Omega}|^2} \right) \right] \\
&\equiv \xi.
\end{aligned} \tag{3.19}$$

Here, ω is the z-component of the vorticity vector that involves only the transverse components of velocity and ξ therefore represents the source term for the vorticity equation. Because the boundary conditions for u and v are homogeneous, (3.19) will be satisfied by the trivial solution $u = v = 0$ only if ξ is identically zero. This can occur in two ways. First, note that ξ is proportional to the reduced second normal stress coefficient d. Thus, if the suspension were Newtonian ($d = 0$), the secondary currents would vanish as expected. Alternatively, even for non-zero values of d, secondary currents vanish if the director derivative terms in ξ are zero by symmetry. This occurs for the geometries in table 1. For geometries which lack this symmetry (e.g. rectangular ducts, elliptical tubes), non-zero second normal stress differences must give rise to secondary currents.

To appreciate the role of the director derivative term, consider the curvature term $-\alpha d\tau/r$ in the particle flux balance equation for a circular tube at steady state, (2.21), which is the analogue of the terms on the right-hand side in (3.18a) and (3.18b). This term is directly proportional to the second normal stress difference coefficient d, the local particle pressure $\alpha\tau$ and inversely proportional to the local radius of streamsurface curvature. This term, which is responsible for the sharper particle migration towards the tube centre in anisotropic suspensions, also represents the forcing function for the secondary currents and establishes a force that drives a
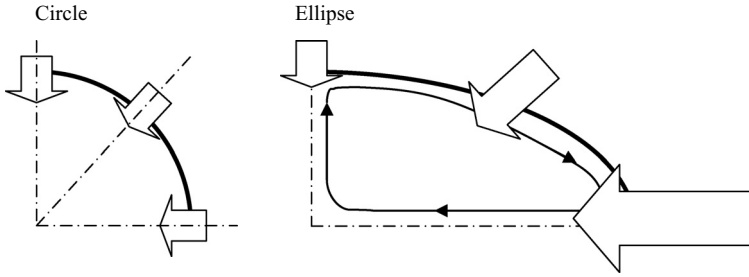
FIGURE 2. Explanation of the origin of the secondary flow in an ellipse. The relative sizes of the arrows (not to any scale) convey the driving force for circulation in the conduits represented by the curvature term in (2.21). (*a*) For the circular cross-section, the driving force is identical in all directions and therefore there is zero net circulation in the geometry. (*b*) For the elliptical cross-section, the driving force from the shallow side regions is the strongest and therefore produces a secondary current that flows towards the centre of the geometry along the major axis and back to the sides along the top (and bottom) walls.

flow along the local radial vector normal to the axial streamsurfaces. For the tube geometry, this driving force is identical from all directions, i.e. the driving force is invariant in the θ-direction (figure 2) and therefore there is zero net flow in the cross-section. However, when there is a lack of symmetry in the cross-section, as would occur with the introduction of an eccentricity to the circle, this term produces a net force that drives circulation currents. Since the driving force is directly proportional to the local curvature, the anisotropic particle stress terms drive a stronger flow from the side regions of the ellipse than from the top and bottom of the ellipse. This results in a non-zero secondary current that flows in from the side regions along the major axis of the ellipse and flows back along the minor axis and the top and bottom walls.

To arrive at a scaling for the magnitude of the circulation velocity, let us examine the solution of the momentum equations in (3.16) for different geometries, beginning with the elliptical geometry. The length scale B used for non-dimensionalization is the semi-minor axis of the ellipse, while W is the ratio of the major axis to the minor axis. The quantity $\psi/(-d)\alpha$, where the streamfunction ψ is obtained by solving the equation (for this and subsequent geometries)

$$\nabla^2\psi = -\frac{1}{\langle w \rangle}\left(\frac{\partial v}{\partial x} - \frac{\partial u}{\partial y}\right), \qquad (3.20)$$

is shown in figure 3 for different aspect ratios. ψ is set to 0 at all boundaries in the cross-section. For the uniform concentration distribution assumed here, the magnitude of the average circulation velocity u_{CIRC} scales as

$$u_{CIRC} = \langle\sqrt{u^2 + v^2}\rangle = (-d)k\alpha U, \qquad (3.21)$$

where U is the average axial velocity $\langle w \rangle$ of the suspension through the tube and k is a scalar that is a function of the geometry of the channel only.

In figure 4, we have shown the variation of k with the inverse of the aspect ratio $1/W$ for the elliptical geometry. As the aspect ratio is increased, k increases and reaches a maximum value of order 10^{-2} when the aspect ratio is roughly 2. This increase is due to the disruption of symmetry provided by the introduction of the second length scale in the cross-section. If the aspect ratio is increased further, k decreases and assumes an asymptotic value of zero as the aspect ratio tends to infinity. The flow is driven by the suspension anisotropy and the gradient in the
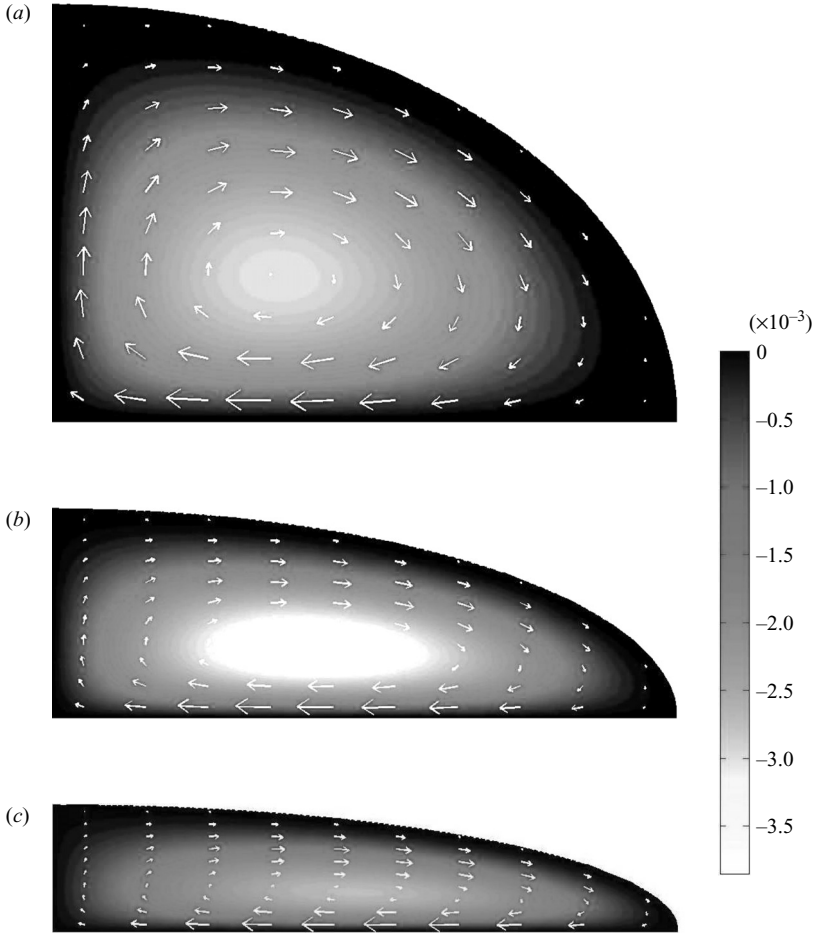
FIGURE 3. Normalized streamfunction $\psi(x, y)/(-d)\alpha(\phi_f)$ (contour profile) and secondary current profiles $[u(x, y), v(x, y)]$ (quiver profile) assuming the concentration distribution to be constant at ϕ_f (a) $W = 1.5$, (b) $W = 3.0$, (c) $W = 5.0$. The profiles are shown over one quarter (first quadrant) of the ellipse.

directors describing the flow geometry. Since the difference in these directors from the centre to the side regions of the conduit is fixed, increasing the horizontal length scale decreases the magnitude of the gradient and hence the magnitude of the secondary current. Examination of the streamfunction depicted in figure 3 shows that the shape of the velocity distribution is roughly independent of the aspect ratio; rather, the magnitude simply vanishes as $1/W$ or $1 - 1/W$ approach zero.

The numerical value of $(-d)k\alpha$ is also of interest as it represents the ratio of the circulation velocity to that of the mean flow. The distance L that the suspension is convected in the axial direction during the time required for the transverse circulation in the cell scales roughly as

$$\frac{L}{B} \sim \frac{1}{(-d)k\alpha}, \qquad (3.22)$$

where B is the characteristic depth of the channel. Since α is $O(1)$ for reasonably concentrated suspensions (e.g. $\alpha(\phi = 0.45) \sim 0.6$) and $k \sim 10^{-2}$, L is approximately
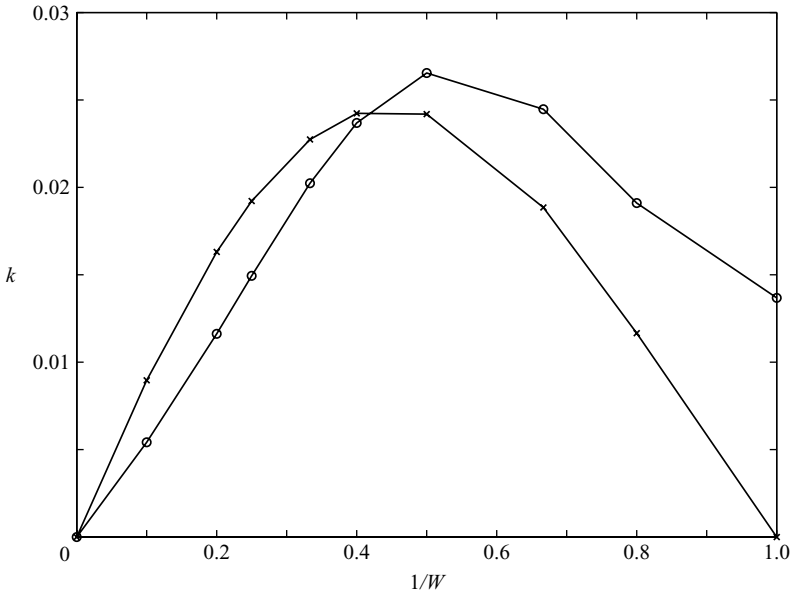
FIGURE 4. The function k as defined in (3.21) as a function of the inverse of the aspect ratio of the conduit $1/W$. Results for ○, rectangles and ×, ellipses of different aspect ratios.

$O(10^2)$ times the channel depth. Thus, as in the case of polymeric systems, the secondary flow is apparent only for very long conduits. Since such aspect ratios are natural in microfluidic channels, secondary currents are more likely to be detected in these systems.

Now consider flow through a rectangular channel. The length scale B used for non-dimensionalizing the equations is the half-depth of the channel, while W is the aspect ratio of the rectangle. The variation of k with the aspect ratio is superficially similar to that of elliptical channels. As shown in figure 4, k has a maximum at an aspect ratio of around 2. Examination of the streamfunction profiles depicted in figure 5, however, shows that there are two circulation cells in each quadrant rather than the single circulation cell in elliptical geometries. In general, the streamline curvature is largest near the corners, weakest near the top and bottom walls at the centre, and intermediate near the sidewalls. For a square channel ($W = 1$), the two circulation flows from the sidewalls and the top and bottom walls are identical, and a secondary flow pattern with 8 equal cells is set up in the cross-section. For large aspect ratios, the flow in the side regions reaches an asymptote with a weak circulation cell adjacent to the sidewall and a stronger cell promoting convection towards the centre. Because this convection dies off exponentially away from the side regions, the overall average magnitude of the convection vanishes as $1/W \to 0$.

It must be noted here that the secondary flow profiles observed experimentally in polymer literature for elliptical (e.g. Giesekus 1965), square (e.g. Dodson *et al.* 1974; Debbaut *et al.* 1997; Debbaut & Dooley 1999) and rectangular (e.g. Debbaut *et al.* 1997) ducts appear to be qualitatively the same as those discussed here for suspension flow, although the constitutive equations governing the secondary flow in polymers are completely different. The number of cells and the direction of flow in figures 3 and 5 for the elliptical and rectangular geometries observed for suspensions are identical
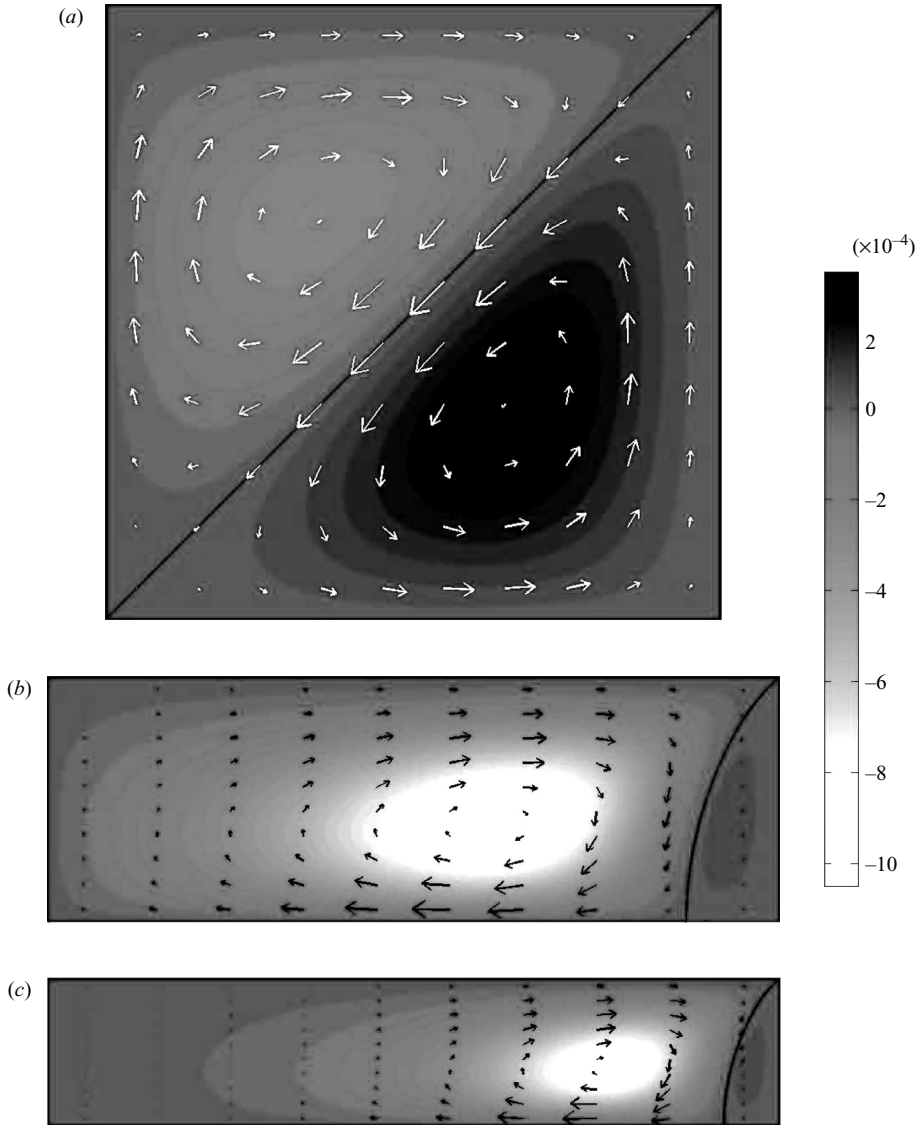
FIGURE 5. Normalized streamfunction $\psi(x, y)/(-d)\alpha(\phi_f)$ (contour profile) and secondary current profiles $[u(x, y), v(x, y)]$ (quiver profile) assuming the concentration distribution to be constant at ϕ_f for a rectangular cross-section of aspect ratio W (a) $W = 1$, (b) $W = 3$, (c) $W = 5$. The separating streamlines are indicated by bold black lines. The profiles are shown over one quarter (first quadrant) of the cross-section.

to what has been observed experimentally and theoretically for viscoelastic polymers, and the magnitudes are again proportional to the second normal stress difference.

Consider a comparison of the scalings of the shear-induced migration velocity and the circulation velocity. From the definition of the flux due to shear-induced migration in (2.6), the shear-induced migration velocity scales as

$$u_{SIM} = U \frac{a^2}{B^2} \frac{f\alpha\mu_r}{\phi_f}. \tag{3.23}$$
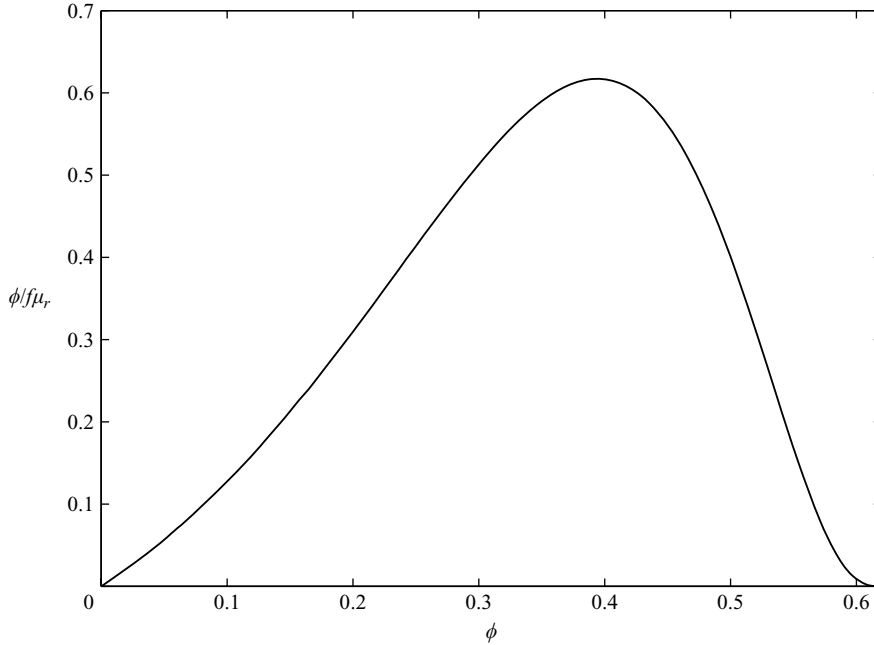
FIGURE 6. The function $\phi/f\mu_r$, which is directly related to the ratio of the scalings of the secondary current and the shear-induced migration velocity as defined in (3.24).

The circulation velocity relative to the shear-induced migration velocity of the particle is then

$$\frac{u_{CIRC}}{u_{SIM}} = (-d)k\frac{B^2}{a^2}\frac{\phi_f}{f\mu_r}. \tag{3.24}$$

In figure 6, we have shown $\phi_f/f\mu_r$, the concentration-dependent part of the right-hand side of (3.24). At low concentrations, the function asymptotes to zero because the second normal stress difference driving the secondary flow goes to zero in the dilute limit faster than the shear-induced migration velocity of the particles. For very large concentrations, the shear-induced migration velocity again dominates the circulation velocity owing to its stronger dependence on concentration. The function shows a maximum value of O(1) at around 40 % average concentration. Therefore, for the circulation velocity to have the same magnitude as the shear-induced migration velocity, the quantity $(-d)kB^2/a^2$ should be $O(1)$, i.e. the Péclet number B^2/a^2 should be $O(100)$, since $(-d)k$ is of order 10^{-2}. For example, the circulation velocity relative to the shear-induced migration velocity has a value of 3 at 40 % concentration for a B/a ratio of just 20. This indicates that the circulation currents can be comparable or even stronger than the shear-induced migration velocities at high Péclet numbers. For vanishingly small particles, shear-induced migration is negligible, but the effect of the secondary flow still persists. The flow average or bulk concentration in most of the simulations in this paper is taken as 0.4 in order to capture the maximum effect of the secondary currents.

4. Concentration and velocity distributions for different geometries

4.1. *Governing equations and solution procedure*

In §3, we eliminated the governing equation for particle distribution from the analysis by assuming that $\phi(x, y) = \phi_f$ in the limit of negligible shear-induced migration, which is appropriate when the axial length of the conduit L is much smaller than the shear-induced migration length scale B^3/a^2. Here, we examine the opposite limit of the particle distribution for finite Péclet numbers when $L \gg B^3/a^2$. To do this, in addition to solving the continuity, (3.2), and momentum, (3.15), equations, we must obtain the solution to the steady-state particle flux balance equation.

For general flows, the following flux balance equation must be solved to determine the concentration distribution

$$\frac{\partial \phi}{\partial t} + \frac{\partial N_i}{\partial x_i} = 0. \tag{4.1}$$

Time is rendered dimensionless with the diffusive scaling $\mu_0 B/Ga^2$. The particle flux vector N_i comprises the convective and diffusive contributions shown in (2.6),

$$N_i = \chi u_i \phi + N_{D_i}, \tag{4.2}$$

where N_D is the shear-induced diffusive flux vector.

$$N_{D_i} = \tfrac{2}{9} f \frac{\partial \Sigma_{ij}^p}{\partial x_j} = -\tfrac{2}{9} f \frac{\partial \alpha \tau H_{ij}}{\partial x_j} + \tfrac{2}{9} f \frac{\partial}{\partial x_j} [2(\mu_r - 1)e_{ij}]. \tag{4.3}$$

The hindered settling factor, f, is modelled by the Richardson–Zaki correlation.

$$f(\phi) = (1 - \phi)^{5.1}. \tag{4.4}$$

Here we use the exponent 5.1 employed by Chapman & Leighton (1991). The shear-induced migration Péclet number χ is given by

$$\chi = \frac{B^2/[(U_c/B)a^2)]}{B/U_c} = \frac{B^2}{a^2}, \tag{4.5}$$

which may be interpreted as the ratio of the shear-induced diffusive time scale to the convective time scale, both defined in (4.5) with respect to the characteristic length scale B of the conduit.

In this paper, we are restricting our analysis to axially invariant flows in the steady asymptotic limit $L \gg B^3/a^2$. In this limit, the particle conservation equation reduces to

$$\chi \left(u \frac{\partial \phi}{\partial x} + v \frac{\partial \phi}{\partial y} \right) + \frac{\partial N_{D_1}}{\partial x} + \frac{\partial N_{D_2}}{\partial y} = 0. \tag{4.6}$$

Since we are considering particle flux within the cross-section of the conduit, the deviatoric stress term in (4.3) involves gradients of the transverse velocity components only. We have already seen in §3 that although the secondary velocity components have the same scaling as the axial velocity, they are numerically three orders of magnitude smaller. Therefore the effect of the secondary currents on the particle stress is negligible, and to a high degree of approximation we may take the shear-induced diffusive flux vector N_D as

$$N_{D_i} = \tfrac{2}{9} f \frac{\partial \Sigma_{ij}^p}{\partial x_j} \approx -\tfrac{2}{9} f \frac{\partial \alpha \tau H_{ij}}{\partial x_j}, \tag{4.7}$$

where τ and H_{ij} may be calculated solely from the axial flow field $w(x, y)$. On the other hand, the convective term involving the transverse velocity must be preserved because it is multiplied by the scaling χ, (4.5), which is usually kept high in experiments (10^2 or greater) in order to enable the modelling of the suspension as a continuum. Thus, the particle flux can be reduced to

$$N_i = \chi u_i \phi - \tfrac{2}{9} f \frac{\partial \alpha \tau H_{ij}}{\partial x_j}. \qquad (4.8)$$

The boundary condition for the concentration balance equation is the zero-flux condition normal to the walls. The velocity field $[u, v, w]$ satisfies the no-slip condition on the walls, which is justified for moderate concentrations and large B/a ratios. For high concentrations or smaller B/a, these boundary conditions could be modified by the introduction of wall slip (e.g. Jana, Kapoor & Acrivos 1995). Such a modification, however, is beyond the scope of this paper.

The steady concentration and velocity distributions can be computed either by integrating (4.6) forward in the axial coordinate z as an entrance flow problem (e.g. Shauly *et al.* 1997; Miller & Morris 2006) or by integrating (4.1) forward in time as an axially invariant start-up flow problem (e.g. Zhang & Acrivos 1994; Tirumkudulu 2001) until the profiles become fully developed. Unfortunately, this is difficult for complex geometries owing to singularities in the constitutive equations at zero shear stress regions in the flow, such as at the centre of a tube. While various fixes for this problem have been used (e.g. Nott & Brady 1994; Zhang & Acrivos 1994; Morris & Boulay 1999), here we side-step these problems by employing the iterative algorithm discussed in Ramachandran & Leighton (2007). All the computations in this paper were performed using the linear solvers in COMSOL 3.2.

In the subsections below, we will discuss the steady-state concentration and velocity profiles for different geometries by comparing three cases: (i) the isotropic model, (ii) the anisotropic model with the shear-induced migration Péclet number χ set to 0 and (iii) the anisotropic model again, but with a finite χ appropriately chosen to elucidate the effect of the secondary currents. Although the $\chi = 0$ case is non-physical (this would require a particle size infinitely greater than the conduit size), we still display the results for this asymptotic case, as it represents the limit when secondary currents are turned off, but the anisotropy-induced particle migration is not. It should be noted here that the area average concentration ($\phi_a = \int\!\int \phi \mathrm{d}S / \int\!\int \mathrm{d}S$) is not conserved for the three cases. This is because the simulations have been performed not for a fixed area average concentration ϕ_a, but for a fixed flow average or bulk concentration ($\phi_f = \int\!\int w \phi \mathrm{d}S / \int\!\int w \mathrm{d}S$). The integrations in the definitions of these average concentrations are carried out over the cross-section of the geometry.

4.2. *Wedge-shaped channels*

A simple geometry that demonstrates the strong effect of circulation within the cross-section on the concentration profile is the wedge geometry (figure 7). In this geometry, the depth varies linearly along the x-direction. The aspect ratio of the wedge is W, and the depth of the shallow end is h times that of the deep end. For large aspect ratios, the depth-averaged velocity at any position scales as the square of the thickness of the wedge at that position, while the stress scales directly as the wedge thickness. Therefore, intuitively, we should expect migration of particles from the thick high-shear-stress regions of the wedge to the thin low-shear-stress regions of the wedge, leading to a high concentration of particles in the thin regions. This is exactly what is predicted by the isotropic model as can be seen from figures 8(*a*) and 9(*a*) for a wedge
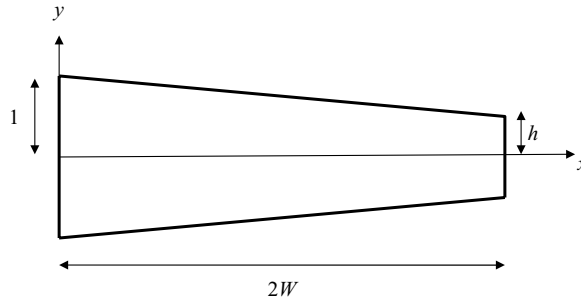
FIGURE 7. Conduit with trapezoidal cross-section of aspect ratio W. The shallow side of the wedge is a factor h times the deep side.
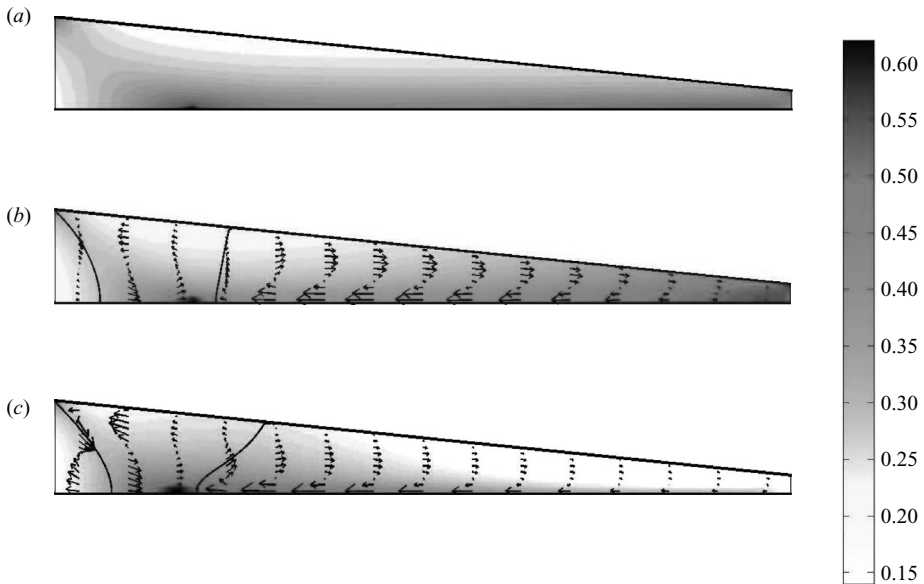

FIGURE 8. Concentration (contour plot) and secondary current (quiver plot) profiles for the wedge geometry ($W = 4, h = 0.2$) computed using the isotropic model (a) and with the anisotropic model with (b) $\chi = 0$ and (c) $\chi = 250$. The profiles are shown over the top half of the cross-section.

with an aspect ratio of 4 and a change of depth of 80 % over this width ($h = 0.2$) at a flow average concentration of 30 %. Since the thin regions also move with slower average velocities, the area average concentration is 0.29, which is greater than the value of 0.28 calculated for a plain rectangular channel with the same mean depth. If we compute the distributions with the anisotropic model, but with the Péclet number set to zero to include just the migration effects of the anisotropy of the particle stress, then the concentration in the shallow regions increases further (see figures 8b and 9b) yielding an area average concentration of 0.31, which is greater than the bulk concentration ($\phi_f = 0.3$). If the complete effect of the anisotropy of the particle stress (to include both secondary currents and particle diffusion) is considered by setting the Péclet number to 250 (figure 8c), it is observed that the particles actually migrate out of the shallow regions into the deeper regions of the channel, a trend completely opposite to what is predicted by previous models. Because of the asymmetry provided
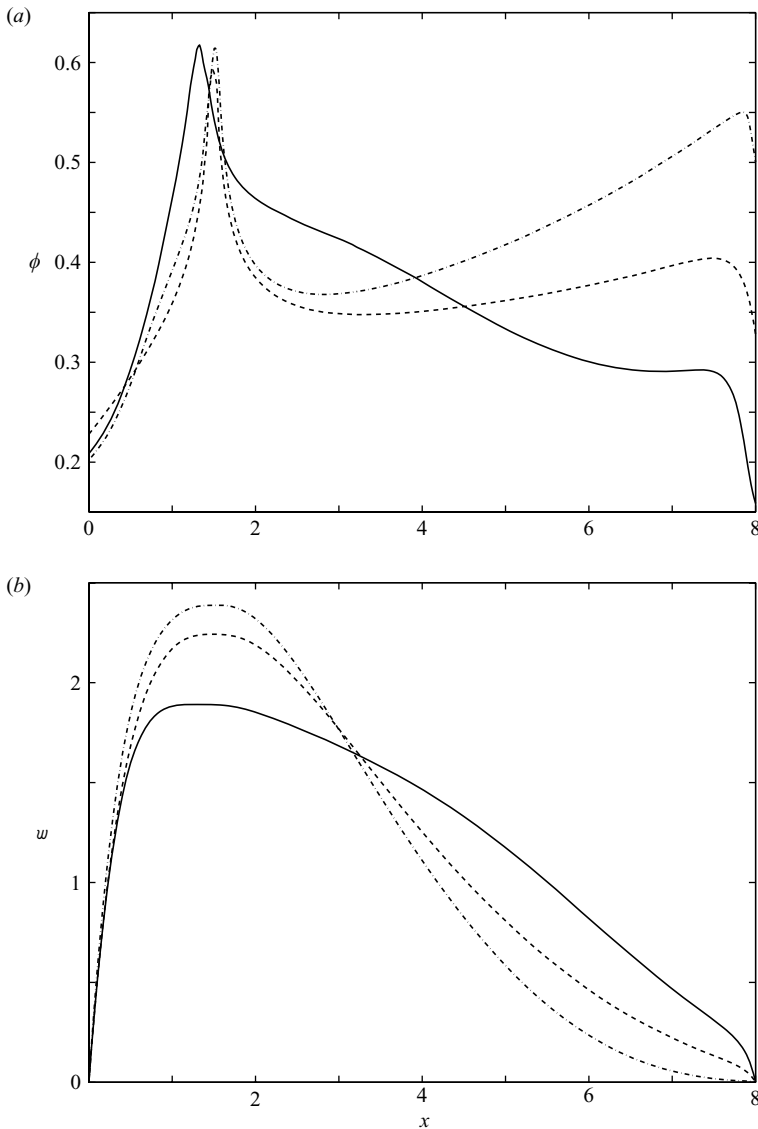
(a)

(b)

FIGURE 9. (a) Axial concentration ($\phi(x, 0)$) and (b) velocity ($w(x, 0)/\langle w \rangle$) profiles along the wedge axis for the isotropic model (dashed line) and for the anisotropic model with $\chi = 0$ (dash-dotted line) and $\chi = 250$ (solid line). The wedge has an aspect ratio of 4 over which the change in depth is 80 % ($h = 0.2$).

by the wedge shape of the cross-section, transverse currents induced by the anisotropy of the particle stress tensor pump particles from the thin regions out into the thicker regions of the wedge, yielding an area average concentration of 0.27. As can be seen from figure 9(a), the concentration near the shallow region (before the sharp drop near the right-hand edge) for the isotropic model is around 40 %, that predicted by the anisotropic model for $\chi = 0$ is 55 %, while for $\chi = 250$, this concentration is just 28 %. We anticipate that for larger Péclet numbers, this draining of particles out of the side pockets of the wedge will be stronger. In figure 10, we have shown the variation of the concentration maximum near the shallow region as a function of the
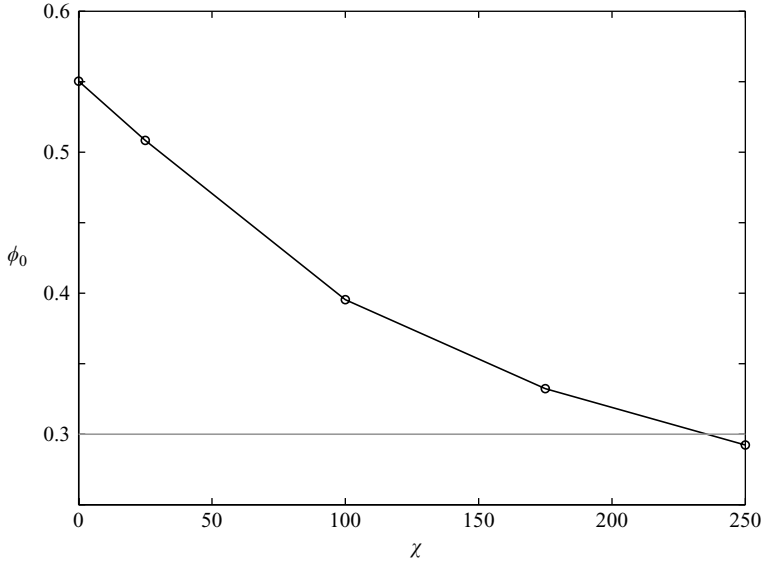
FIGURE 10. The concentration maximum along the midplane near the shallow end of the wedge ($W = 4, h = 0.2$) as a function of the Péclet number. As can be seen from the graph, the concentration is much higher than the bulk concentration (30 %, shown by the horizontal line) for $\chi = 0$, but decreases gradually as the Péclet number is increased and eventually drops below the bulk concentration for a Péclet number of approximately 235.

Péclet number. This figure clearly shows the changing nature of the shallow region from being a pocket of high concentration to being a pocket of low concentration with increase in Péclet number. As a result of this transition, the velocity profiles become progressively more blunted with increase in the Péclet number (figure 9*b*).

4.3. *Elliptical channels*

Consider the elliptical channel of aspect ratio W. The length scale B chosen to define χ is the semi-minor axis of the ellipse. In figure 11, we have shown the concentration contours and the secondary velocity profiles for the flow of a 40 % suspension ($\phi_f = 0.4$) in an elliptical channel of aspect ratio 2 for the isotropic model and the anisotropic model with $\chi = 0$ and $\chi = 1600$. Shear-induced migration results in the diffusion of particles from the top and bottom of the tube towards the midplane (major axis) of the ellipse. The second normal stress induces a convection from the high-curvature regions near the sides towards the centre. At high χ (e.g. figure 11*c*), the combination of these effects results in a significant depletion of particles from the side regions. This effect is more clearly seen in figure 12, where we have plotted the concentration distribution along the major axis of the ellipse. For $\chi = 1600$, the particles are convected from the sidewalls towards the centre of the ellipse more strongly relative to the isotropic and the $\chi = 0$ concentration profiles, causing a 'shoulder' in the profile. The concentration predicted by the isotropic model near the sidewall is around 37 %, while that predicted by the anisotropic model at $\chi = 1600$ is just 27 %. The depletion near the sidewall with respect to the 40 % flow average concentration is thus nearly four times that predicted by the isotropic model. The axial velocity $w/\langle w \rangle$ along the major axis is shown for the three cases in figure 12(*b*). While very similar, the velocity profile for the anisotropic model with $\chi = 1600$
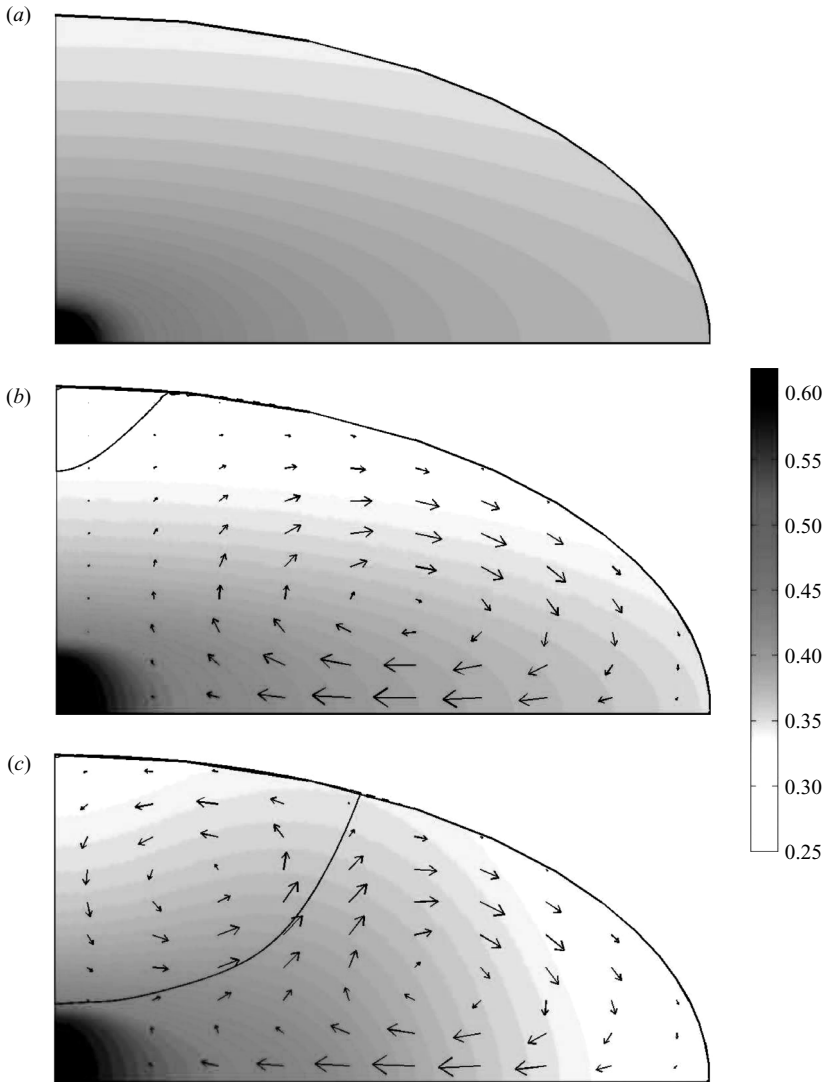
FIGURE 11. Concentration ϕ (contour profile) and secondary current profiles $[u, v]$ (quiver profile) for the elliptical geometry with an aspect ratio of 2 computed using the isotropic model (a) and the anisotropic model with (b) $\chi = 0$ and (c) $\chi = 1600$. The profiles are shown over one quarter (first quadrant) of the ellipse.

shows the maximum blunting among the three owing to the stronger migration of the particles towards the centre.

For an aspect ratio of 2 and a flow average concentration of 40%, the average circulation velocity $\langle\sqrt{u^2 + v^2}\rangle/\langle w\rangle$ is shown as a function of Péclet number in figure 13. The magnitude of the circulation velocity drops sharply as the Péclet number is increased from zero to small values, and then decreases gradually to a non-zero asymptote for larger values of χ, but the impact of the secondary flow on the concentration profile increases progressively. Since the depth of the channel is small in the side regions, the curvature of the streamlines is greater near the sidewalls than near the centre of the ellipse. This leads to large circulation cells that flow in from the sidewalls to the centre along the horizontal axis and weak circulation cells
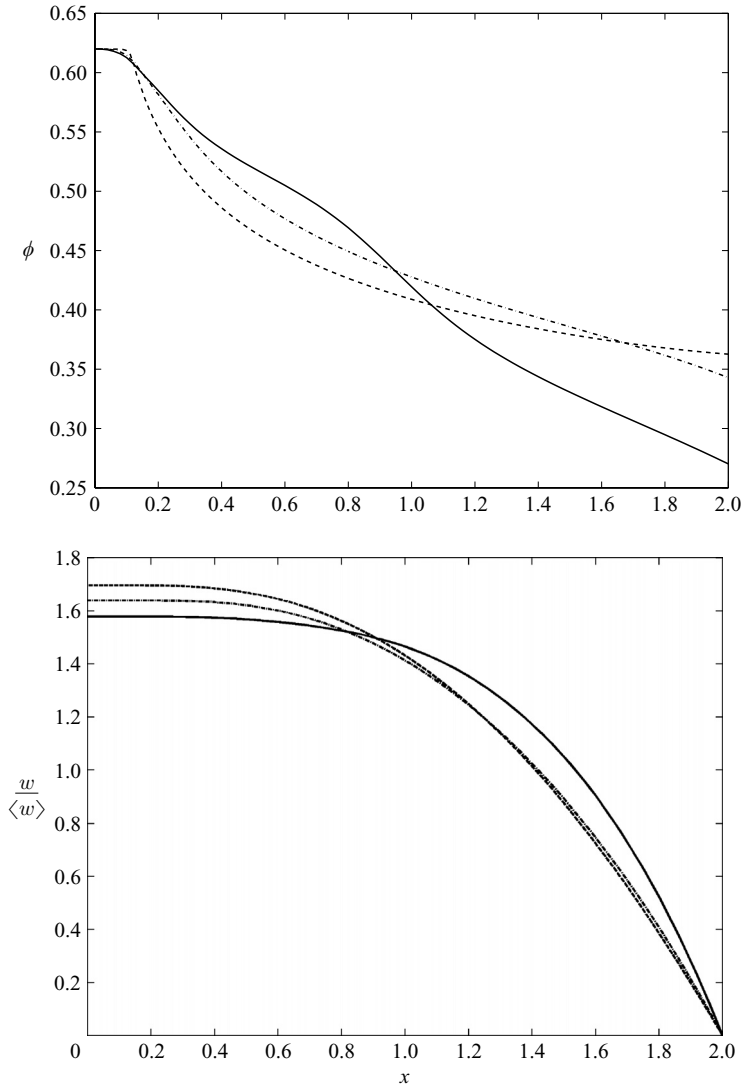
FIGURE 12. (*a*) Concentration $\phi(x, 0)$ and (*b*) axial velocity profiles $w(x, 0)/\langle w \rangle$ along the centreline for the elliptical geometry with an aspect ratio of 2: dash line, isotropic model; dash-doted line, $\chi = 0$; solid line, $\chi = 1600$.

near the top and bottom of the minor axis, resulting in 8 total cells in the cross-section (figure 11), which is twice the number of cells observed in the case of a constant concentration field in §3. As the Péclet number is increased, the depletion of particles from the side regions leads to a relative decrease in the driving force for the cell along the major axis since this driving force is directly related to α, a monotonically increasing function of concentration. This results in a decrease in the size of this cell and an increase in the size of the cell along the minor axis with increase in Péclet number. The interaction of the two convection cells leads to a stretching out of the high-concentration region along the dividing streamline (see figure 11*c*).

Next, we examine the variation of the concentration and velocity distributions with the average concentration ϕ_f. We see in figure 14 that the magnitude of the
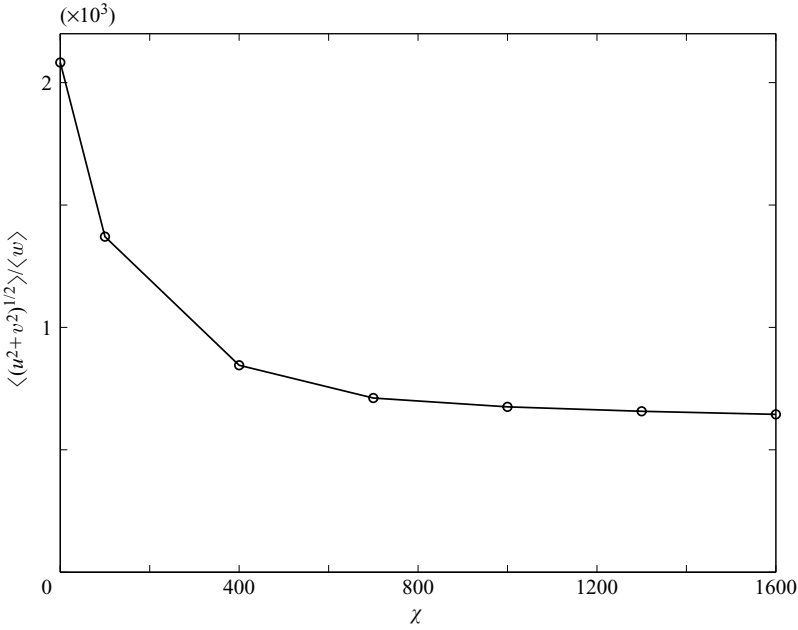
FIGURE 13. The variation of the average magnitude of the secondary current $\langle\sqrt{u^2+v^2}\rangle/\langle w\rangle$ with χ for an elliptical channel of aspect ratio 2 for $\phi_f = 0.4$.
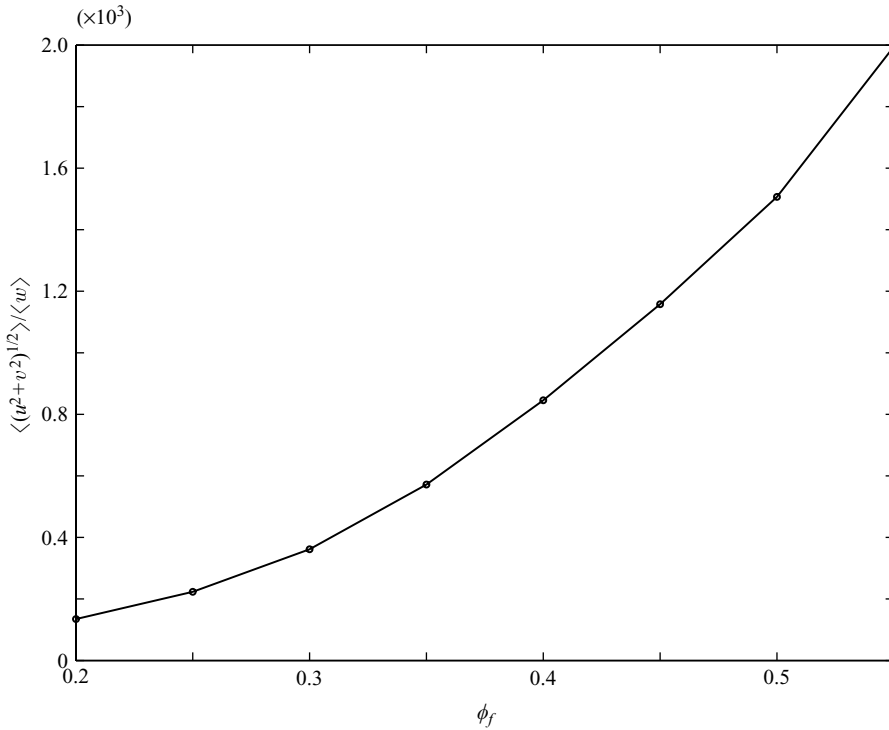

FIGURE 14. Variation of the average magnitude of the secondary currents $\langle\sqrt{u^2+v^2}\rangle/\langle w\rangle$ with the flow average concentration ϕ_f for an elliptical channel of aspect ratio 2 for $\chi = 400$.
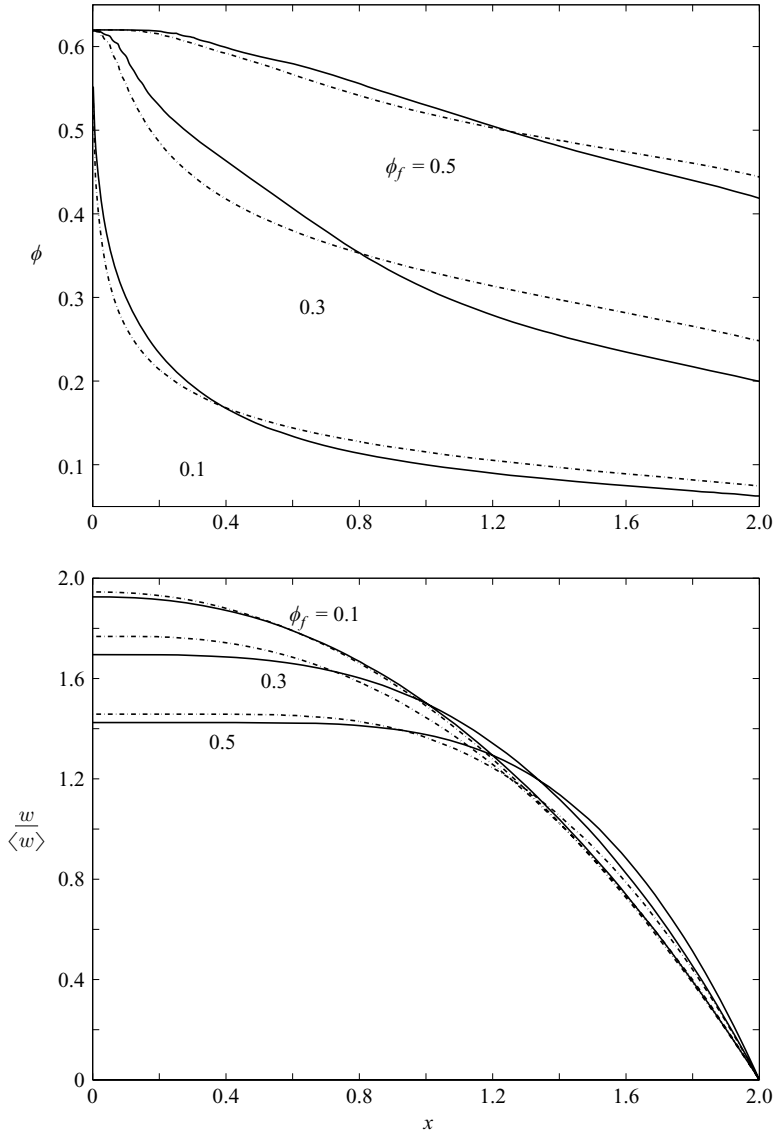
FIGURE 15. (*a*) Concentration [$\phi(x, 0)$] and (*b*) axial velocity [$w(x, 0)/\langle w \rangle$] profiles along the horizontal axis for an elliptical channel of aspect ratio 2 for different flow average concentrations: dash-dotted line, $\chi = 0$; solid line, $\chi = 400$.

secondary currents increases monotonically with concentration, which again is because the secondary currents scale as the reduced normal stress α. In figure 15, we have shown the concentration and axial velocity profiles along the major axis of an ellipse of aspect ratio 2 for $\phi_f = 0.1$, 0.3 and 0.5 at $\chi = 0$ and $\chi = 400$. The deviation between the two curves at $\chi = 0$ and $\chi = 400$ shows the additional segregation produced by the secondary currents. The difference between the curves at the two Péclet numbers is small for the low 10 % and the high 50 % average concentrations and is large for the intermediate 30 % concentration. This can be explained on the basis of the scaling analysis presented in (3.24). For low concentrations, the normal stresses are negligible and therefore there is little difference in the concentration
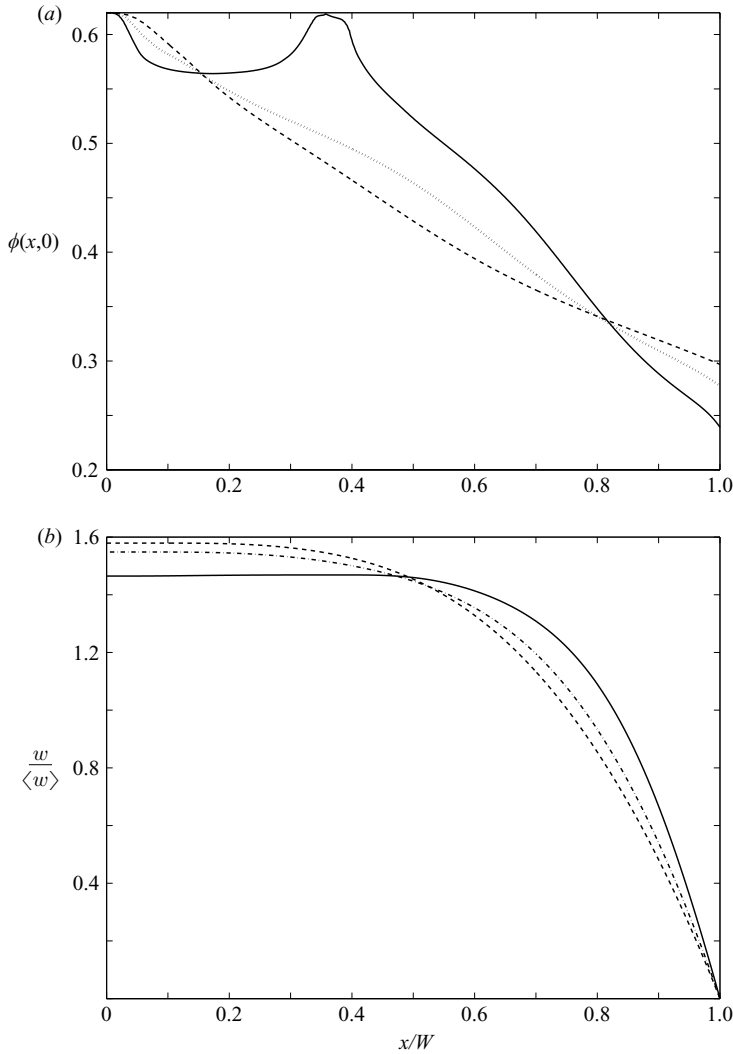
FIGURE 16. (a) Concentration $[\phi(x, 0)]$ and (b) axial velocity $[w(x, 0)/\langle w \rangle]$ profiles along the horizontal axis for elliptical channels of different aspect ratios with $\phi_f = 0.4$ and $\chi = 400$: dashed line, $W = 2$; dash-dotted line, $W = 3$; solid line, $W = 5$.

profile with the inclusion of the secondary currents. At high concentration, shear-induced migration increases more rapidly with concentration than do the secondary currents, thus the effect of convection shows a maximum at intermediate concentrations.

Finally, we study the effect of the aspect ratio of the ellipse on the concentration and velocity distributions. The concentration and axial velocity profiles along the major axis of the ellipse are shown for three different aspect ratios: 2, 3 and 5 in figure 16 for $\chi = 400$. The anisotropic model with $W = 5$ (figure 16c) shows two maxima. This can also be seen in the contour plot of the concentration profile in figure 17 for this aspect ratio. In fact, the concentration variation for $W = 5$ appears to be an abrupt change from the monotonic variations observed for the smaller aspect ratios of 2 and
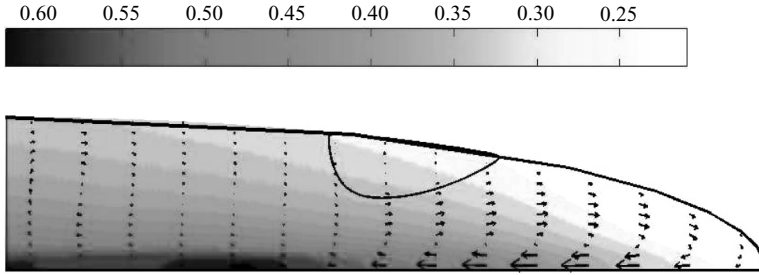
FIGURE 17. Concentration ϕ (contour profile) and secondary current profiles $[u, v]$ (quiver profile) for the elliptical geometry with an aspect ratio of 5 for $\chi = 400$ and $\phi_f = 0.4$. The profiles are shown over one quarter (first quadrant) of the ellipse.

3 in figures 16(a) and 16(b), respectively. The appearance of the two concentration maxima along the major axis of the ellipse is not a numerical artefact, but the result of an instability due to second normal stress difference induced secondary currents. In the limit of large aspect ratios where the effect of the side regions is weak, weak cells are formed away from the side regions whose wavelengths are comparable to the depth of the ellipse. To understand this phenomenon, we turn to the limiting geometry of plane-Poiseuille flow.

4.4. *Plane Poiseuille flow*

Consider the plane Poiseuille flow of a suspension through a rectangular channel without sidewalls. The length scale B used to define χ is the half-depth of the channel. The flow is in the z-direction, y is the thin dimension of channel, and x is the vorticity direction. The theoretical solution of the particle distribution equation for this simple geometry is quite straightforward: $\alpha\tau = $ constant, as noted in §2. Since τ is a function of y only, the concentration profile does not vary in the vorticity direction. Also, this solution is satisfied by the governing equations for all Péclet numbers, because the secondary current is identically zero for this solution. We shall call this solution $\Phi(y)$. At low Péclet numbers, it was possible to retrieve this trivial solution via the iterative solution technique employed earlier in this section (see Ramachandran & Leighton (2007) for details of the technique). However, for Péclet numbers greater than 400, a steady solution with the required tolerance was not accessible with this technique, suggesting that the trivial solution Φ could be unstable at large Péclet numbers.

To investigate the stability of Φ, we integrated the axially invariant version of the time-dependent problem in (4.1) with time to determine the asymptotic behaviour for an area average concentration of 37.5 % and an aspect ratio of 5 at different Péclet numbers. In this start-up flow problem, we circumvented the numerical issue of concentrations exceeding maximum packing by solving for the dependent variable Ψ which is defined as

$$\Psi = \log\left[\frac{\alpha\tau}{2.17\dot{\gamma}}\right]. \tag{4.9}$$

The concentration distribution can be obtained by inverting the above map:

$$\phi = \frac{\phi_m \exp(\Psi/3)}{\phi_m + \exp(\Psi/3)}. \tag{4.10}$$
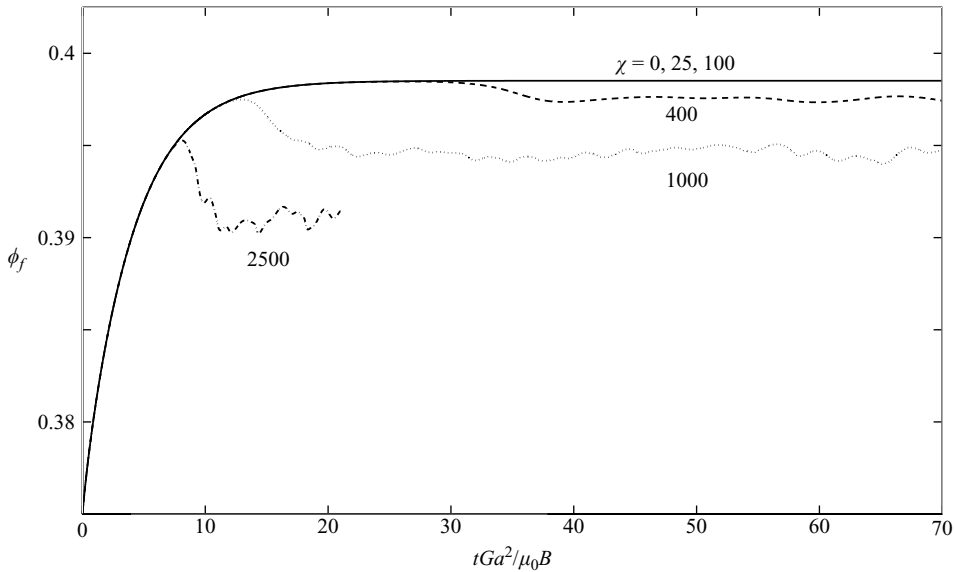
FIGURE 18. The variation of the flow average concentration with time for the start-up flow with an initially uniform concentration distribution ($\phi_a = 0.375$) for different Péclet numbers. For $\chi = 0, 25$ and 100, the flow average concentration curves lie on top of each other and produce the steady-state case of $\alpha\tau = $ constant (solid line). For $\chi = 400, 1000$ and 2500 (dashed dotted and dash-dotted lines, respectively), the flow average concentration curves stay along the $\chi = 0$ initially, but fall off eventually, displaying an oscillatory behaviour.

To avoid complications due to the vanishing shear rates at flow centres, the shear rate $\dot{\gamma}$ was augmented by a constant $\dot{\gamma}_0$, as suggested by Miller & Morris (2006):

$$\dot{\gamma} = \sqrt{w_x^2 + w_y^2 + \dot{\gamma}_0^2}, \tag{4.11}$$

where $\dot{\gamma}_0$ was taken as 10^{-4} in all the simulations. The practical implication of this numerical fix is that concentrations never quite reach maximum packing, but are limited to approximately 58 %. Apart from this, the computed profiles were insensitive to the choice of $\dot{\gamma}_0$. Symmetry boundary conditions were applied at the two side boundaries of the computational domain.

The variation of the flow average concentration with time is shown in figure 18 for a range of Péclet numbers. At $\chi = 0$, the flow average concentration increases with time because of particle migration towards the centreline, and reaches an asymptote. It can be seen that the curves for $\chi = 25$ and 100 lie on top of the curve at $\chi = 0$, which represents the case when secondary currents are turned off. For $\chi = 400$, however, the flow average concentration follows the $\chi = 0$ curve for a short while, and then falls off the curve to exhibit an oscillatory variation. The reduction in the flow average concentration is due to mixing induced by the secondary currents within the cross-section. A similar behaviour is observed at $\chi = 1000$ and $\chi = 2500$. The concentration distributions at $tGa^2/(\mu_0 B) = 50$ for different Péclet numbers are shown in figure 19. The concentration profiles for $\chi = 0, 25$ and 100 are invariant in the vorticity (x) direction, which is consistent with the solution Φ. However, for larger Péclet numbers, the solution is unstable with periodic structures in the x-direction. These periodic structures translate in the x-direction, and thus there is no steady state for these Péclet numbers (see figure 20).
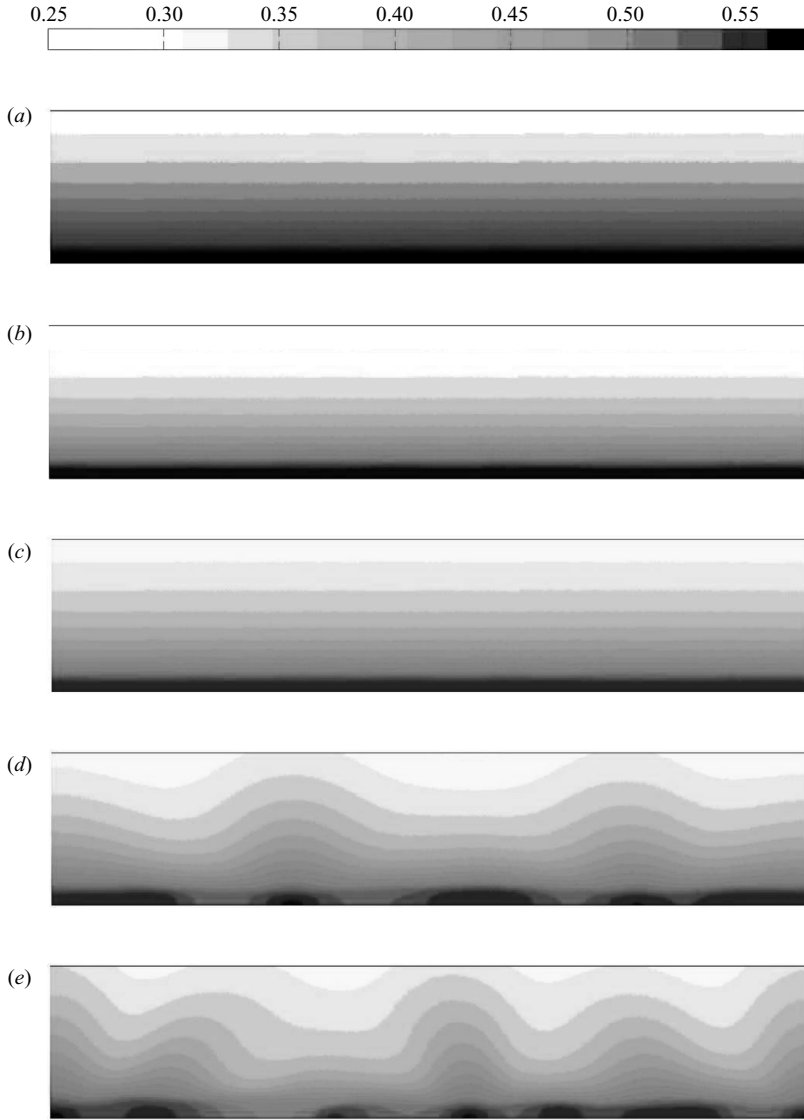
FIGURE 19. The concentration ϕ profiles at $tGa^2/\mu_0 B = 50$ for Péclet numbers of 0, 25, 100, 400 and 1000. The area average concentration is 0.375 for all the simulations. The profiles are shown only for the top half of the channel cross-section.

In retrospect, the instability of Φ at high Péclet numbers should not be surprising, since it has been shown theoretically by Brady & Carpen (2002) that the Couette flow of a combination of a suspension (modelled with constant concentration) and a Newtonian fluid superposed over each other is unstable to spanwise perturbations owing to a jump in the second normal stress difference between the two fluids. It is possible to show using similar modelling that the same is true for plane Poiseuille flow of a suspension and a Newtonian fluid. Performing the complete stability analysis for plane Poiseuille flow of a suspension is beyond the scope of this paper. We make a note of this instability here, however, as it is necessary to understand the steady results for conduits of large aspect ratios.
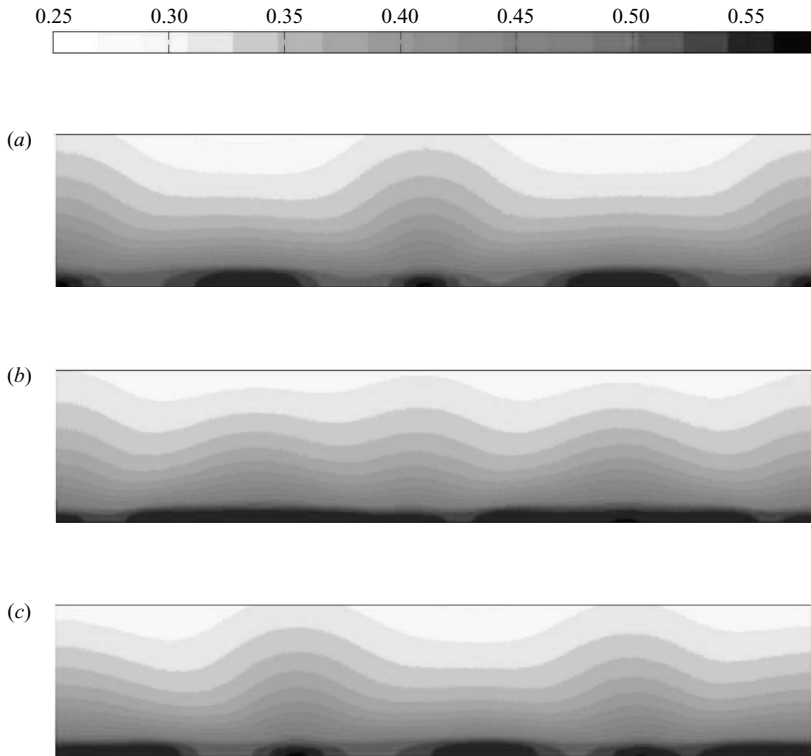
FIGURE 20. The concentration ϕ profiles at a Péclet number of 400 for times $tGa^2/\mu_0 B$ equal to (*a*) 38, (*b*) 44, (*c*) 50. The profiles are shown only for the top half of the channel cross-section. The figures show waves travelling from the centre to both the left and to the right with time.

4.5. *Rectangular channels*

Consider the rectangular channel of aspect ratio W. The length scale B used to define χ is the half-depth of the channel. In figure 21, we have shown the concentration and secondary current profiles along the horizontal symmetry axis of a rectangular channel with an aspect ratio of $W = 2$ at a flow average concentration of 40%. As seen in the case of the ellipse, the concentration profiles are shifted away from the sidewalls towards the centre of the channel for the anisotropic model relative to the isotropic model. For large Péclet numbers (e.g. $\chi = 1000$ as shown in the figure), we observe the emergence of a second maximum in the concentration. This can be seen more clearly in figure 22, where we have shown the contours of the concentration and velocity profiles for $\chi = 0$, 400 and 1000, for $\phi_f = 0.4$ and aspect ratio of $W = 2$. The secondary maximum is driven by the same curvature effects that produce the instability at high χ for unbounded plane Poiseuille flow. For the rectangular channel at small aspect ratios, however, the presence of the sidewalls fixes the location of the maximum in the channel and convergence is observed even at $\chi = 1000$. Note that the concentration between the two concentration maxima varies from around 58% to maximum packing, which is not large compared to the variation between the concentrations at the wall and near the centre of the channel. Therefore, it is unlikely that these concentration maxima will be accessible by experiment.

Next, we investigate the effect of aspect ratio on the concentration and secondary current profiles in figure 23 with $\phi_f = 0.4$ and $\chi = 100$. Note that this Péclet number
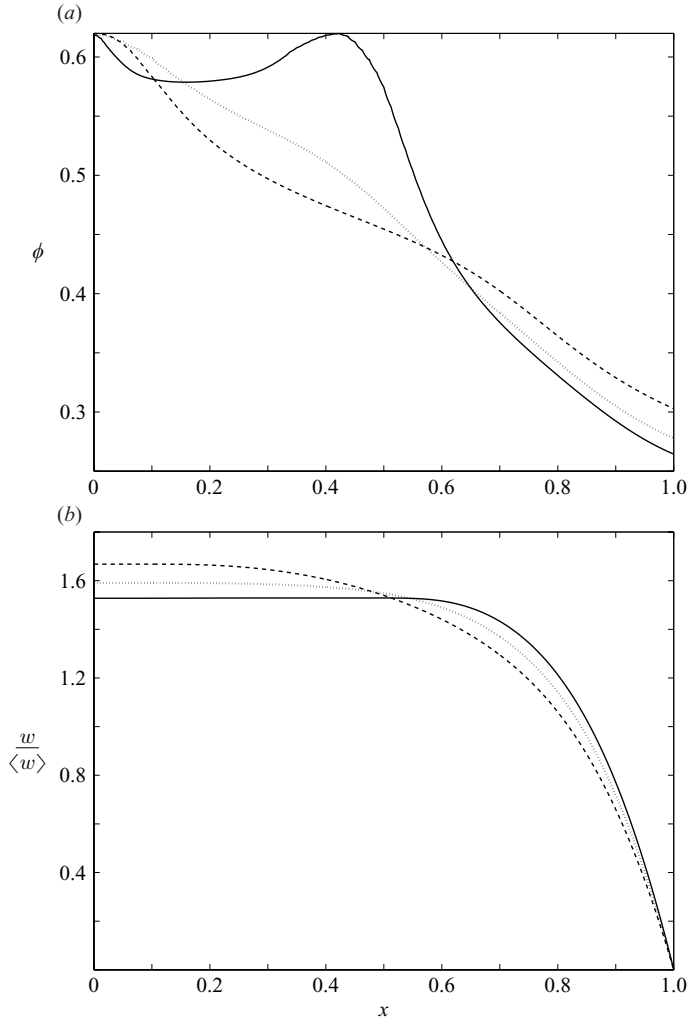
FIGURE 21. (*a*) Concentration and (*b*) axial velocity profiles along the horizontal axis $\phi(x, 0)$ for the rectangular channel with aspect ratio $W = 2$ and $\phi_f = 0.4$ for the isotropic model (dashed line) and the anisotropic model with $\chi = 400$ (dash-dotted line) and $\chi = 1000$ (solid line).

is well below the critical Péclet number for the onset of the instability in unbounded plane Poiseuille flow, and thus convergent steady solutions could be obtained at all aspect ratios. For low aspect ratios, there are three circulation cells in each quadrant of the rectangle. For the uniform concentration asymptote considered in §3, there are only two cells per quadrant. The third cell at the top of the channel, similar to the one observed in the case of the ellipse, appears because of the competition between the driving forces for circulation near the channel top and bottom and the channel sides. As the aspect ratio increases, this third cell decreases in size and eventually vanishes owing to negligible curvature of the axial streamsurfaces in this region. For large aspect ratios (e.g. figure 23*c*) at this small Péclet number, a secondary maximum is observed near the sidewalls from both the iterative and time-dependent solutions.
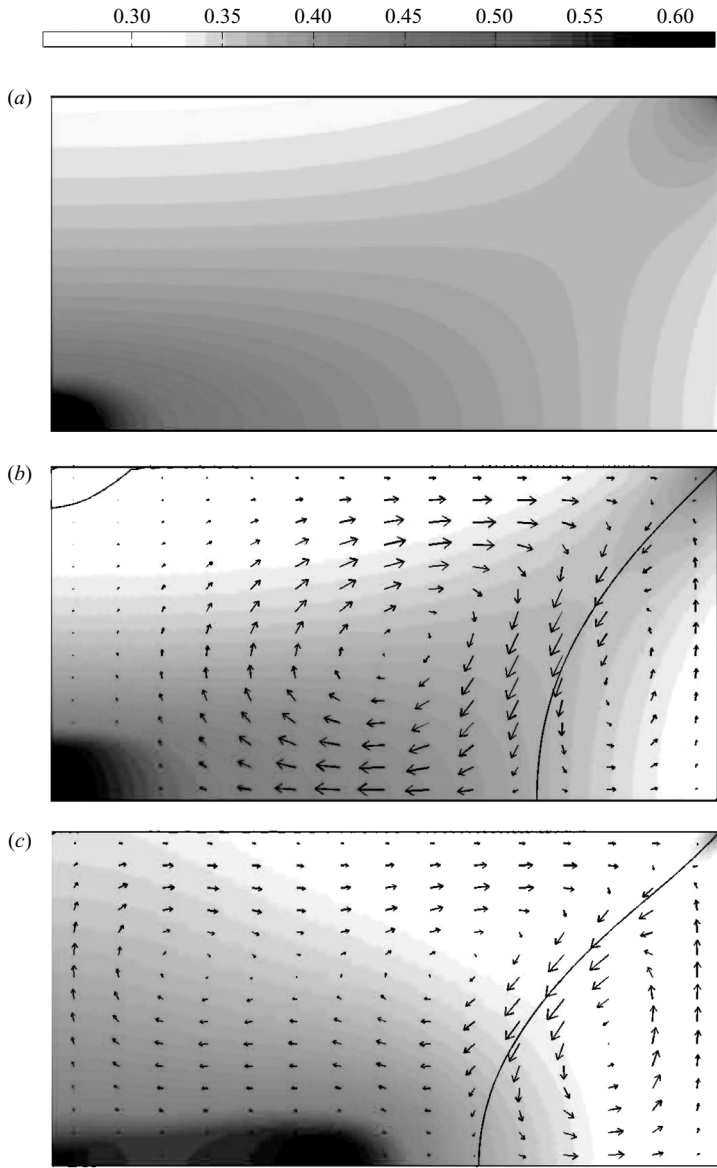
FIGURE 22. Concentration ϕ and secondary current profiles $[u, v]$ (quiver profile) for a rectangular channel with an aspect ratio of 2 at 40 % bulk concentration for (a) $\chi = 0$, (b) $\chi = 400$, (c) $\chi = 1000$. The profiles are shown over one quarter (first quadrant) of the cross-section.

Thus for low Péclet numbers, the concentration profile obtained is steady, with a secondary maximum obtained at larger aspect ratios.

For high Péclet numbers and large aspect ratios, a steady solution was not obtained with either the iterative or the time-integration techniques. Analogous to the case of plane Poiseuille flow, spatially periodic concentration profiles translate within the cross-section, resulting in an unsteady variation of the flow average concentration for the start-up flow problem.
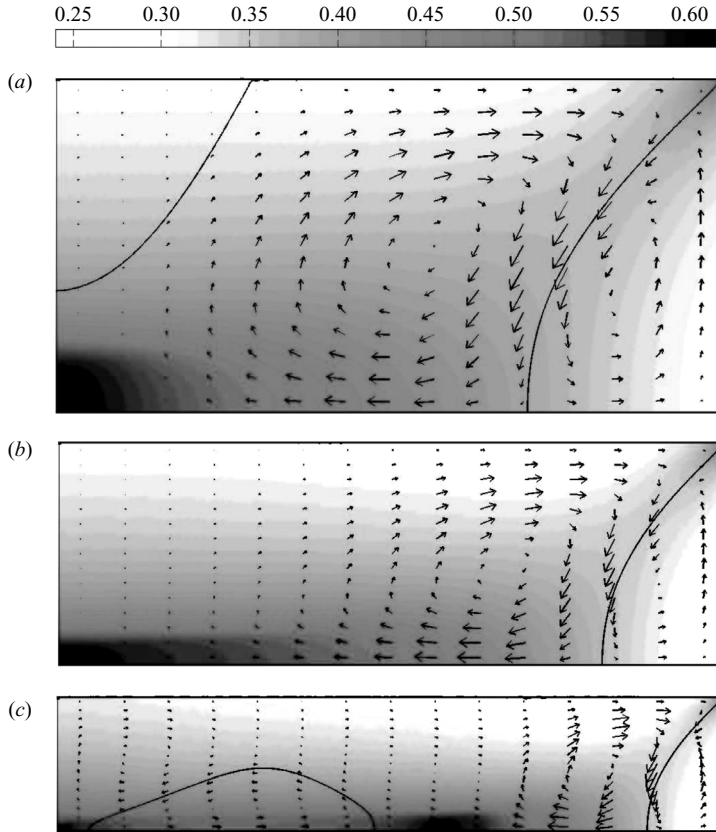
FIGURE 23. Concentration ϕ (contour profile) and secondary current profiles $[u, v]$ (quiver profile) for the rectangular channel with aspect ratios (*a*) $W = 2$, (*b*) $W = 3$ and (*c*) $W = 5$ for $\chi = 100$ and $\phi_f = 0.4$. The profiles are shown over one quarter (first quadrant) of the cross-section.

5. Conclusions

In this paper, the significance of the effect of second normal stress difference induced secondary currents on the steady-state concentration profile for the pressure-driven flow of a suspension through a conduit of arbitrary cross-section is demonstrated through simulations. Traditionally, suspensions have been modelled as isotropic Newtonian fluids with effective viscosities that vary with concentration when calculating the velocity distribution through a conduit. The results presented in this paper, however, show that it is critical to consider the complete non-Newtonian rheology of a concentrated suspension when modelling flows in complex geometries. While the magnitude of the secondary currents due to non-Newtonian effects is small, in many cases they are the dominant mechanism governing the resulting particle concentration distribution and lead to counterintuitive results. For example, it was shown for the wedge geometry that the concentration profile obtained from the isotropic shear-induced migration argument turns out to be the exact opposite of what is obtained in the presence of the secondary flows in the cross-section. Contrary to the prediction that particles should migrate into shallow regions and corners in a geometry on account of their relatively lower average shear stresses, the complete solution of the governing equations shows that secondary currents at high χ actually

flush particles out of these regions. An important implication of this observation is that secondary currents may circumvent the accumulation of particles in the notches and corners of a conduit.

The secondary currents reach their largest magnitudes when the aspect ratio of the conduit is approximately 2. With increase in Péclet number, the magnitude of the secondary currents decreases, but the effect of the secondary currents on the concentration profile increases progressively. The secondary flow effects are most likely to be observed when the average concentration ranges from 30 % to 50 %, when the magnitude of the currents is high relative to the shear-induced migration velocity for reasonably large Péclet numbers.

The concentration distributions for plane Poiseuille flow of a suspension obtained by the time integration of the start-up flow problem are invariant in the vorticity direction only for Péclet numbers below a critical value. Beyond this critical Péclet number, this solution is unstable and the secondary flow induced by second normal stress differences leads to upwelling and downwelling regions, producing concentration maxima and minima. Also, these upwelling and downwelling regions are found to translate within the cross-section, and thus these solutions are unsteady.

The origin of the secondary currents in the flow of suspensions through conduits at steady state is attributed to the asymmetry caused by an azimuthal gradient in the curvature of the flow streamsurfaces such as occurs in any non-axisymmetric flow. This source of asymmetry is weak and leads to small magnitudes of the circulation currents. Therefore, the effects of these currents is realized only at high Péclet numbers. Because conduits are typically 10 to 50 particle diameters across, however, the Péclet number in experiments usually ranges from 100 to 2500, leading secondary currents to dominate the migration process. The breaking of symmetry due to the presence of a body force such as gravity is much stronger, and hence the impact of the secondary currents is more pronounced in such cases. In a related paper (Ramachandran & Leighton 2007), we have discussed the effect of the second normal stress difference induced secondary currents on the concentration and velocity profiles in the classic tube resuspension geometry and demonstrate that the experimentally observed profiles can be reproduced nearly quantitatively using the anisotropic model discussed in this paper. To the best of our knowledge, such secondary currents and their resulting effect on concentration profiles have not yet been observed for neutrally buoyant suspensions.

As is well known, in the absence of both secondary currents and wall-slip effects, the steady concentration distribution of a suspension flowing through a straight conduit of arbitrary cross-section is independent of the particle size. With the inclusion of non-Newtonian secondary currents, however, we have shown that there is a pronounced effect of the size ratio B/a for all non-axisymmetric flows.

REFERENCES

ABBOTT, J. R., TETLOW, N., GRAHAM, A. L., ALTOBELLI, S. A., FUKUSHIMA, E., MONDY, L. A. & STEPHENS, T. S. 1991 Experimental observations of particle migration in concentration suspensions: Couette flow. *J. Rheol.* **35**, 773–795.

ACRIVOS, A., MAURI, R. & FAN, X. 1993 Shear-induced resuspension in a Couette device. *Intl J. Multiphase Flow* **19**, 797–802.

ALTOBELLI, S. A., GIVLER, R. C. & FUKUSHIMA, E. 1991 Velocity and concentration measurements of suspensions by nuclear magnetic resonance imaging. *J. Rheol.* **35**, 721–734.

BRADY, J. F. & CARPEN, I. E. 2002 Second normal stress jump instability in non-Newtonian fluids. *J. Non-Newtonian Fluid Mech.* **102**, 219–232.

BRICKER, J. M. & BUTLER, J. E. 2006 Oscillatory shear of suspensions of non-colloidal particles. *J. Rheol.* **50**, 711–728.

CHAPMAN, B. K. 1990 Shear-induced migration phenomena in suspensions. PhD thesis, University of Notre Dame.

CHAPMAN, B. K. & LEIGHTON, D. T. 1991 Dynamic viscous resuspension. *Intl J. Multiphase Flow* **17**, 469–483.

CHOW, A. W., SINTON, S. W., IWAMIYA, J. H. & STEPHENS, T. S. 1994 Shear-induced particle migration in Couette and parallel-plate viscometers: NMR imaging and stress measurement. *Phys. Fluids* **6** (8), 2561–2576.

CHOW, A. W., SINTON, A. W., IWAMIYA, J. H. & LEIGHTON, D. T. 1995 Particle migration of non-Brownian concentrated suspensions in a truncated cone and plate. Poster at Society of Rheology meeting.

DACUNHA, F. R. & HINCH, E. J. 1996 Shear-induced dispersion in a dilute suspension of rough spheres. *J. Fluid Mech.* **309**, 211–223.

DEBBAUT, B. & DOOLEY, J. 1999 Secondary motions in straight and tapered channels: experiments and three-dimensional finite element simulation with a multimode differential viscoelastic model. *J. Rheol.* **43**, 1525–1545.

DEBBAUT, B., AVALOSSE, T., DOOLEY, J. & HUGHES, K. 1997 On the development of secondary motions in straight channels induced by the second normal stress difference: experiments and simulations. *J. Non-Newtonian Fluid Mech.* **69**, 255–271.

DODSON, A. G., TOWNSEND, P. & WALTERS, K. 1974 Non-Newtonian flow in pipes of non-circular cross-section. *Computers Fluids* **19**, 317–338.

FANG, Z., MAMMOLI, A. A., BRADY, J. F., INGBER, M. S., MONDY, L. A. & GRAHAM, A. L. 2002 Flow-aligned tensor models for suspension flows. *Intl J. Multiphase Flow* **28**, 137–166.

GIESEKUS, H. 1965 Sekundarstromungen in viskoelastischen Flussigkeiten bei stationarer und periodischer Bewegung. *Rheol. Acta* **4**, 85–101.

GREEN, A. E. & RIVLIN, R. S. 1956 Steady flow of non-Newtonian fluids through tubes. *Q. Appl. Maths* **14**, 229–308.

HAMPTON, R. E., MAMMOLI, A. A., GRAHAM, A. L. & TETLOW, N. 1997 Migration of particles undergoing pressure-driven flow in a circular conduit. *J. Rheol.* **41**, 621–640.

JANA, S. C., KAPOOR, B. & ACRIVOS, A. 1995 Apparent wall slip velocity coefficients in concentrated suspensions of noncolloidal particles. *J. Rheol.* **39**, 1123–1132.

JENKINS, J. T. & MCTIGUE, D. F. 1990 *Two Phase Flows and Waves*, pp. 70–79. Springer.

KOH, C. J., HOOKHAM, P. & LEAL, L. G. 1994 An experimental investigation of concentrated suspension flows in a rectangular channel. *J. Fluid Mech.* **266**, 1–32.

KRISHNAN, G. P., BEIMFOHR, S. & LEIGHTON, D. T. 1996 Shear-induced radial segregation in bidisperse suspensions. *J. Fluid Mech.* **321**, 371–393.

LEIGHTON, D. & ACRIVOS, A. 1986 Viscous resuspension. *Chem. Engng Sci.* **41**, 1377–1384.

LEIGHTON, D. & ACRIVOS, A. 1987 The shear-induced migration of particles in concentrated suspensions. *J. Fluid Mech.* **181**, 415–439.

LYON, M. K. & LEAL, L. G. 1998 An experimental study of the motion of concentrated suspensions in two-dimensional channel flow. Part 1. Monodisperse systems. *J. Fluid Mech.* **363**, 25–56.

MERHI, D., LEMAIRE, E., BOSSIS, G. & MOUKALLED, F. 2005 Particle migration in a concentrated suspension flowing between rotating parallel plates: investigation of diffusion flux coefficients. *J. Rheol.* **49**, 1429–1448.

MILLER, R. M. & MORRIS, J. F. 2006 Normal stress-driven migration and axial development in pressure-driven flow of concentrated suspensions. *J. Non-Newtonian Fluid Mech.* **135** (2-3), 149–165.

MILLS, P. & SNABRE, P. 1995 Rheology and structure of concentrated suspension of hard spheres: shear-induced particle migration. *J. de Phys.* II **5**, 1597–1608.

MORRIS, J. F. & BOULAY, F. 1999 Curvilinear flows of non-colloidal suspensions: the role of normal stresses. *J. Rheol.* **43**, 1213–1237.

NORMAN, J. T., NAYAK, H. V. & BONNECAZE, R. T. 2005 Migration of buoyant particles in low Reynolds number pressure-driven flows. *J. Fluid Mech.* **523**, 1–35.

NOTT, P. R. & BRADY, J. F. 1994 Pressure-driven flow of suspensions: simulations and theory. *J. Fluid Mech.* **275**, 157–199.

PHAN-THIEN, N. 1995 Constitutive equation for concentrated suspensions in Newtonian liquids. *J. Rheol.* **39**, 679–695.

PHILLIPS, R. J., ARMSTRONG, R. C., BROWN, R. A., GRAHAM, A. L. & ABBOTT, J. R. 1992 A constitutive model for concentrated suspensions that accounts for shear-induced particle migration. *Phys. Fluids* A **4**, 30–40.

RAMACHANDRAN, A. & LEIGHTON, D. T. 2007 Viscous resuspension in a tube: the impact of secondary flows resulting from second normal stress differences. *Phys. Fluids* **19** (5), 055301.

SCHAFLINGER, U., ACRIVOS, A. & ZHANG, K. 1990 Viscous resuspension of a sediment within a laminar and stratified flow. *Intl J. Multiphase Flow* **16**, 567–578.

SEMJONOW, V. 1967 Sekundarstromungen hochpolymerer Schmelzen in einem Rohr von elliptischem Querschnitt. *Rheol. Acta* **6**, 171–173.

SHAPLEY, N., ARMSTRONG, R. C. & BROWN, R. A. 2002 Laser doppler velocimetry measurements of particle velocity fluctuations in a concentrated suspension. *J. Rheol.* **46**, 241–272.

SHAULY, A., AVERBAKH, A., NIR, A. & SEMIAT, R. 1997 Slow viscous flows of highly concentrated suspensions: Part II – particle migration, velocity and concentration profiles in rectangular ducts. *Intl J. Multiphase Flow* **23**, 613–629.

SMART, J. & LEIGHTON, D. T. 1989 Measurement of the hydrodynamic surface roughness of noncolloidal spheres. *Phys. Fluids* A **1** (1), 52–60.

TETLOW, N., GRAHAM, A. L., INGBER, M. S., SUBIA, S. R., MONDY, L. A. & ALTOBELLI, S. A. 1998 Particle migration in a Couette apparatus: experiment and modeling. *J. Rheol.* **42**, 307–327.

TIRUMKUDULU, M. S. 2001 Viscous resuspension and particle segregation in concentrated suspensions undergoing shear. PhD thesis, City University of New York.

TRIPATHI, A. 1998 Experimental investigations of shear-induced particle migration in concentrated suspensions undergoing shear. PhD thesis, University of New York.

ZARRAGA, I. E. & LEIGHTON, D. T. 2001 Normal stress and diffusion in a dilute suspension of hard spheres undergoing simple shear. *Phys. Fluids* **13**, 565–577.

ZARRAGA, I. E., HILL, D. A. & LEIGHTON, D. T. 2000 The characterization of the total stress of concentrated suspensions of noncolloidal spheres in Newtonian fluids. *J. Rheol.* **44**, 185–220.

ZHANG, K. & ACRIVOS, A. 1994 Viscous resuspension in fully developed laminar pipe flows. *Intl J. Multiphase Flow* **20**, 579–591.